Check for updates

Local Wall Cooling Effects on Hypersonic Boundary-Layer Stability

Furkan Oz* and Thomas E. Goebel†
Oklahoma State University, Stillwater, Oklahoma 74078
Joseph S. Jewell‡
Purdue University, West Lafayette, Indiana 47907
and
Kursat Kara§
Oklahoma State University, Stillwater, Oklahoma 74078

https://doi.org/10.2514/1.A35404

Hypersonic boundary-layer stability has significant importance in vehicle design and successful operation. This paper investigates the stabilization effects of local wall cooling on the hypersonic boundary layers over a 5 deg half-angle blunt cone with a nose radius of 0.0254 mm. We employed a high-order-accurate flow solver to calculate the steady flow for a freestream Mach number of 6.0 and a unit Reynolds number of 25.59×10^6/m. In simulations, we considered partial wall cooling, entire wall cooling, and adiabatic wall scenarios. Furthermore, we examined partial cooling parameters such as strip location, length, and temperature profiles. We calculated the growth rates, phase speed, and N-factor diagrams using a linear stability analysis. The results showed that complete wall cooling destabilizes the boundary layer. However, the cooling strip upstream of the synchronization point stabilized the boundary layer by damping the disturbances. The longer cooling strip further stabilized the boundary layer. The cooling strip placed downstream of the synchronization point destabilized the boundary layer.

Downloaded by OKLAHOMA STATE UNIVERSITY on October 28, 2022 | http://arc.aiaa.org | DOI: 10.2514/1.A35404

Nomenclature

A, B	=	inviscid flux vectors in the axial and radial directions
A_v, B_v	=	viscous flux vectors in the axial and radial directions
c	=	phase speed
c_p, c_v	=	specific heat at constant pressure and volume
E	=	total energy
e	=	molecular internal energy
F	=	dimensionless frequency
f	=	dimensional frequency
J	=	Jacobian matrix
k	=	thermal conductivity
M	=	Mach number
N	=	empirical number for e^N method
p	=	pressure
Pr	=	Prandtl number
Q	=	state vector
q	=	heat flux
Re	=	Reynolds number
S	=	source term
u, v, w	=	velocity components in x, y, and z directions
x, y	=	two-dimensional coordinates
x, y, z	=	three-dimensional coordinates
x, y, θ	=	axisymmetric coordinates
α, β	=	wave number in x and z directions
μ	=	dynamic viscosity
ν	=	kinematic viscosity
ξ, η	=	curvilinear coordinates
ρ	=	density
σ	=	growth rate
τ	=	shear stress
ω	=	angular frequency

Subscripts

ad	=	adiabatic wall condition
e	=	boundary-layer edge condition
i	=	imaginary component of a complex number
tr	=	transition onset location
w	=	wall condition
∞	=	freestream condition

Received 26 February 2022; revision received 30 August 2022; accepted for publication 7 September 2022; published online Open Access 25 October 2022. Copyright © 2022 by the authors. Published by the American Institute of Aeronautics and Astronautics, Inc., with permission. All requests for copying and permission to reprint should be submitted to CCC at www.copyright.com; employ the eISSN 1533-6794 to initiate your request. See also AIAA Rights and Permissions www.aiaa.org/randp.

*Graduate Student, School of Mechanical and Aerospace Engineering; foz@okstate.edu. Student Member AIAA.

†Undergraduate Student, School of Mechanical and Aerospace Engineering.

‡Assistant Professor, School of Aeronautics and Astronautics. Associate Fellow AIAA.

§Assistant Professor, School of Mechanical and Aerospace Engineering; kursat.kara@okstate.edu. Senior Member AIAA (Corresponding Author).

I. Introduction

HYPERSONIC boundary-layer transition from the laminar to the turbulent state is crucial for efficient hypersonic vehicle design. Key effects include an increase in the aerodynamic heating [1,2]. This heat transfer increment may require a heavier and more expensive thermal protection system, potentially including active cooling or thicker material [3]. Moreover, viscous drag (which represents up to 50% of the total drag [4,5]) increases in turbulent flow. Besides these effects, the boundary-layer transition affects the overall vehicle operability and maintenance requirements, including more frequent refurbishment or replacement of thermal protection system materials. A transition control system capable of stabilizing boundary-layer transition to reduce the aforementioned critical effects is therefore of great interest.

Although transition mechanisms in hypersonic flow are not completely understood, especially for complex geometries, previous research has shown that there are at least two different paths from a laminar to a turbulent hypersonic boundary-layer state. If the surface of the body is smooth enough and the freestream environment is quiet (in order words, relatively disturbance-free), the first path can occur. This path includes receptivity, which is the mechanism of very small disturbances entering the laminar boundary-layer, generating waves [6], the linear phase, and nonlinear breakdown to turbulence [7]. Linear stability theory (LST) [8] provides a model for how small unstable disturbances are amplified in the linear phase. The disturbances reach a critical level and trigger nonlinear breakdown to

Downloaded by OKLAHOMA STATE UNIVERSITY on October 28, 2022 | http://arc.aiaa.org | DOI: 10.2514/1.A35404

turbulence. In the second path, which can occur in the presence of large freestream disturbances or rough surfaces, the linear phase is bypassed and freestream disturbances grow nonlinearly.

The Mach number, Reynolds number, vehicle geometry, and initial amplitude are the main parameters that affect the evolution and breakdown of the instability waves. The complex flow environment and the disturbance field growing in the hypersonic boundary layer are illustrated in Fig. 1. In this figure, three different types of disturbances (acoustic, vorticity, and entropy) come from the interaction of the main shock wave with environmental disturbances [9].

As linear stability theory explains, in a disturbance-free environment, transition to turbulence occurs because instabilities are amplified within the boundary layer. The first and second Mack instability modes are directly related to the local Reynolds number in a two-dimensional hypersonic boundary layer. It is crucial to stabilize these modes to delay and control the transition process. Research has mostly focused on these modes to facilitate transition control. Although the second mode is the dominant instability mode in the hypersonic boundary layer for many slender geometries with low wall-temperature ratios, it can be stabilized with an ultrasonically absorptive coating (UAC) [10–19]. Fedorov et al. [11] showed that the UAC can significantly stabilize the second mode, and subsequent transition can therefore be delayed. Experimental studies [20–23] verified this model and showed that the UAC can stabilize the second mode. However, this approach slightly destabilizes the first mode.

The first mode can be stabilized with full wall cooling; however, the second and higher modes will be destabilized at hypersonic speeds [24–31]. As a result, in hypersonic flow where the second mode is dominant, full wall cooling is not an optimum method to use as laminar boundary-layer control. The destabilizing behavior of the full wall cooling can be significantly mitigated with local wall cooling/heating. In supersonic flow, Masad and Abid [32] used local heating to stabilize the first mode in Mach 3.5 flow. More recently, Polivanov et al. [33] numerically investigated the effect of the local cooling/heating strips on the stability behavior of the hypersonic boundary layer. Their study used a sharp cone in Mach 6 flow. They revealed that the local cooling delays the transition and decreases the second-mode amplitude. Moreover, they also concluded that the neutral point is a critical factor in stabilizing behavior. The effect of the cooling strip can be reversed by the location with respect to the neutral point. After Polivanov et al., Soudakov et al. [34] used different locations for local cooling and heating to investigate the mode amplification and to determine the transition onset point. Although Soudakov et al.'s results agree with Polivanov et al.'s results [33], they stated that the e^N method based on the local stability analysis may be misleading because of the highly nonuniform regions around the local cooling/heating strips.

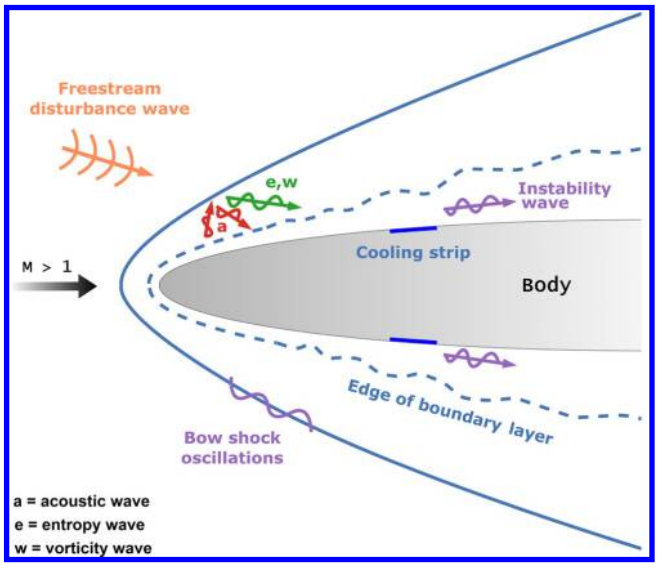

Fig. 1 Schematic illustration of the complex flow physics and boundary-layer development.

Fedorov et al. [35] and Sidorenko et al. [36] investigated the effect of local cooling/heating in a Mach 6 flow for a sharp cone. They numerically and experimentally investigated the stability behavior. The results indicate that the local cooling delays the transition, and their results were in agreement with the previous findings. They stated that the local cooling stabilizes the second mode, unlike the full cooling. Additionally, the local heating shifted the transition upstream in their experiment.

Zhao et al. [37] numerically investigated the effect of local cooling/heating on the synchronization point. Their simulations over the flat plate with Mach 6 flow revealed local cooling leads to boundary-layer thickness change; as a result, the position of the synchronization points moves at a specific frequency. One notable finding from the study is that a second synchronization point is formed when the cooling strip is located downstream of the adiabatic case's neutral point location. Recently, Batista and Kuehl [38] investigated the combination of both heating and cooling strips numerically. They used Purdue University's flared cone geometry [39] at Mach 6 flow conditions. Their findings indicate that the most effective way to stabilize the hypersonic boundary layer is to place a cooling strip upstream and to place a heating strip downstream.

In the present study, the aim is to apply both local and full cooling to investigate and compare the effect of the local cooling with various cooling profiles and full cooling on the hypersonic boundary-layer stability. A 5 deg half-angle cone with $R = 0.0254$ mm (0.001 in.) nose bluntness is used at a freestream Mach number of $M = 6$ with a cooling strip. The steady flow was solved by a compressible Navier–Stokes solver code that uses the fifth-order-accurate weighted essentially nonoscillatory (WENO) scheme [40] for spatial discretization and a third-order total variation diminishing (TVD) Runge–Kutta scheme [41] for time integration. Linear stability theory was then applied to the steady flow solution. The cooling process was imposed with different profiles and temperatures.

II. Governing Equations

A. Steady Flow

The equations solved are unsteady, compressible, axisymmetric Navier–Stokes equations in conservative form, as shown in the following:

$$\frac{\partial Q}{\partial t} + \frac{\partial A}{\partial x} + \frac{\partial B}{\partial y} = \frac{\partial A_v}{\partial x} + \frac{\partial B_v}{\partial y} + S \tag{1}$$

where Q is the state vector, and A and B are the axial- and radial-direction inviscid flux vectors given by

$$Q = \begin{bmatrix} \rho \\ \rho u \\ \rho v \\ \rho E \end{bmatrix}, \; A = \begin{bmatrix} \rho u \\ \rho u^2 + p \\ \rho uv \\ (\rho E + p)u \end{bmatrix}, \; B = \begin{bmatrix} \rho v \\ \rho vu \\ \rho v^2 + p \\ (\rho E + p)v \end{bmatrix} \tag{2}$$

A_v and B_v are the axial- and radial-direction viscous and heat conduction flux vectors given by

$$A_v = \begin{bmatrix} 0 \\ \tau_{xx} \\ \tau_{xy} \\ u\tau_{xx} + v\tau_{xy} - q_x \end{bmatrix}, B_v = \begin{bmatrix} 0 \\ \tau_{yx} \\ \tau_{yy} \\ u\tau_{yx} + v\tau_{yy} - q_y \end{bmatrix} \tag{3}$$

The vector S contains source terms resulting from the axisymmetric formulation. The source term, viscous stresses, and heat fluxes have the following forms:

$$S = \frac{1}{y}\left\{ \begin{bmatrix} 0 \\ \tau_{yx} \\ \tau_{yy} - \tau_{\theta\theta} \\ u\tau_{yx} + v\tau_{yy} - q_y \end{bmatrix} - \begin{bmatrix} \rho v \\ \rho uv \\ \rho v^2 \\ (\rho E + p)v \end{bmatrix} \right\} \tag{4}$$

$$\tau_{xx} = \frac{2}{3}\frac{\mu}{Re}\left(2\frac{\partial u}{\partial x} - \frac{\partial v}{\partial y} - \frac{v}{y}\right) \tag{5}$$

$$\tau_{yy} = \frac{2}{3}\frac{\mu}{Re}\left(2\frac{\partial v}{\partial y} - \frac{\partial u}{\partial x} - \frac{v}{y}\right) \tag{6}$$

$$\tau_{\theta\theta} = \frac{2}{3}\frac{\mu}{Re}\left(2\frac{v}{y} - \frac{\partial u}{\partial x} - \frac{\partial v}{\partial y}\right) \tag{7}$$

$$\tau_{xy} = \frac{\mu}{Re}\left(2\frac{\partial u}{\partial y} + \frac{\partial v}{\partial x}\right) \tag{8}$$

$$q_x = -\frac{\gamma}{(\gamma-1)\,\mathrm{Pr}\,Re}\frac{\partial T}{\partial x} \tag{9}$$

$$q_y = -\frac{\gamma}{(\gamma-1)\,\mathrm{Pr}\,Re}\frac{\partial T}{\partial y} \tag{10}$$

A singularity exists along the symmetry axis of $y = 0$. The method for the elimination of the singularity and the derivation of viscous stresses and heat fluxes was described by Kara et al. [42].

The schematic of the computational domain is illustrated in Fig. 2. The computational domain is two-dimensional, and the contribution of the third direction (coming from axisymmetric formulation) is added to the system with the source term S. Here, (x, y) represent the two-dimensional coordinates where (u, v) are the corresponding velocity components, ρ is the density, and p is the pressure. The total energy E is, therefore,

$$E = e + \frac{u^2 + v^2}{2}, \quad e = c_v T, \quad p = \rho \mathrm{RT} \tag{11}$$

Here, e is the molecular internal energy and T is the temperature. The viscosity μ is computed using Sutherland's law with no correction for low temperature, and the coefficient of conductivity is given in terms of the Prandtl number ($\mathrm{Pr} = 0.7$). The variables ρ, p, and T, as well as the velocity, are nondimensionalized by their corresponding reference variables ρ_∞, p_∞, and T_∞, as well as $\sqrt{\mathrm{RT}_\infty}$, respectively. For computational purposes, the equations are transformed from the physical coordinate system (x, y) to a computational curvilinear coordinate system (ξ, η). The calculation of the derivatives in the transformed coordinates is reproduced from the literature [43–45], and interested readers are encouraged to check the aforementioned references for the detailed derivations. Briefly, we define the Jacobian matrix and its inverse as follows:

$$J = \begin{bmatrix} \frac{\partial \xi}{\partial x} & \frac{\partial \xi}{\partial y} \\ \frac{\partial \eta}{\partial x} & \frac{\partial \eta}{\partial y} \end{bmatrix} = \begin{bmatrix} \frac{\partial x}{\partial \xi} & \frac{\partial x}{\partial \eta} \\ \frac{\partial y}{\partial \xi} & \frac{\partial y}{\partial \eta} \end{bmatrix}^{-1} \tag{12}$$

If the inverse on the right-hand side is applied, Eq. (12) can be written as

$$J = \begin{bmatrix} \frac{\partial \xi}{\partial x} & \frac{\partial \xi}{\partial y} \\ \frac{\partial \eta}{\partial x} & \frac{\partial \eta}{\partial y} \end{bmatrix} = \frac{1}{J^*}\begin{bmatrix} \frac{\partial y}{\partial \eta} & -\frac{\partial x}{\partial \eta} \\ -\frac{\partial y}{\partial \xi} & \frac{\partial x}{\partial \xi} \end{bmatrix} \tag{13}$$

where the Jacobian determinant J^* is expressed as

$$J^* = \frac{\partial y}{\partial \eta}\frac{\partial x}{\partial \xi} - \frac{\partial x}{\partial \eta}\frac{\partial y}{\partial \xi} \tag{14}$$

As a result, the derivative transformations expressed in terms of inverse metrics are

$$\frac{\partial}{\partial x} = \frac{1}{J^*}\left[\left(\frac{\partial}{\partial \xi}\right)\left(\frac{\partial y}{\partial \eta}\right) - \left(\frac{\partial}{\partial \eta}\right)\left(\frac{\partial y}{\partial \xi}\right)\right] \tag{15}$$

$$\frac{\partial}{\partial y} = \frac{1}{J^*}\left[\left(\frac{\partial}{\partial \eta}\right)\left(\frac{\partial x}{\partial \xi}\right) - \left(\frac{\partial}{\partial \xi}\right)\left(\frac{\partial x}{\partial \eta}\right)\right] \tag{16}$$

The derivatives of the physical coordinates with respect to transformed coordinates are calculated using the fifth-order essentially nonoscillatory (ENO) method. Our flow solver can import any clustered grid in physical coordinates and calculates the corresponding derivatives using the Jacobian and inverse metrics. The grid used in this study is stretched in the η direction. The finer grid is used in the boundary layer to capture strong gradients accurately. In the ξ direction, the grid is very fine near the nose; and it is uniform in the flat region. We made the data for the computational grid and flow solution for the adiabatic wall case publicly available in the GitHub online database to reproduce the results. Interested readers should see the Appendix to learn more about the dataset. The computational domain extends from $x = -0.81$ to 354 mm in the axial direction, where $x = 0$ corresponds to tip of the blunt cone. The transformed governing equations from the physical coordinate system (x, y) to a computational coordinate system (ξ, η) are

$$\frac{\partial \overline{Q}}{\partial t} + \frac{\partial \overline{A}}{\partial \xi} + \frac{\partial \overline{B}}{\partial \eta} = \frac{\partial \overline{A_v}}{\partial \xi} + \frac{\partial \overline{B_v}}{\partial \eta} + \overline{S} \tag{17}$$

The individual components are

$$\overline{Q} = \frac{Q}{J^*}, \quad \overline{A} = \frac{(\partial \xi/\partial x)A + (\partial \xi/\partial y)B}{J^*}, \quad \overline{B} = \frac{(\partial \eta/\partial x)A + (\partial \eta/\partial y)B}{J^*} \tag{18}$$

$$\overline{A_v} = \frac{(\partial \xi/\partial x)A_v + (\partial \xi/\partial y)B_v}{J^*}, \quad \overline{B_v} = \frac{(\partial \eta/\partial x)A_v + (\partial \eta/\partial y)B_v}{J^*}, \quad \overline{S} = \frac{S}{J^*} \tag{19}$$

The resulting system of equations is solved with a fifth-order-accurate weighted essentially nonoscillatory scheme in spatial discretization and a third-order-accurate total variation diminishing Runge–Kutta (TVD-RK) method in time discretization. These schemes solve the resultant system of equations discretely in a

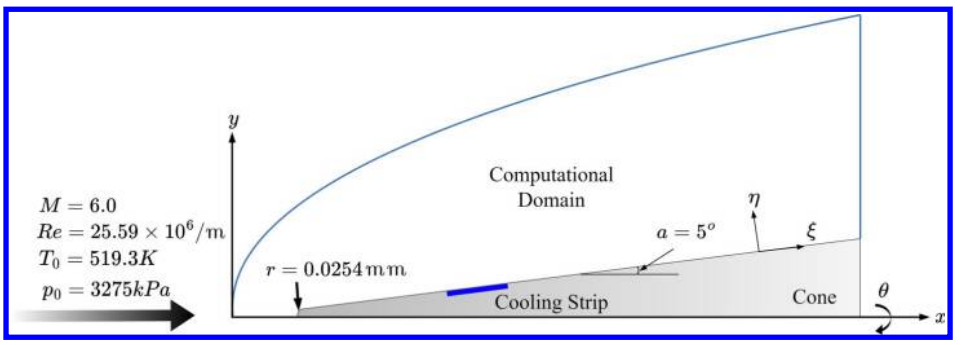

Fig. 2 Schematic illustration of computational domain where (x, y) are physical coordinates and (ξ, η) are computational coordinates.

Downloaded by OKLAHOMA STATE UNIVERSITY on October 28, 2022 | http://arc.aiaa.org | DOI: 10.2514/1.A35404

uniform structured computational domain in which flow properties are known at the grid nodes. The WENO scheme approximates the spatial derivatives in a given direction to a higher order at the nodes by using the neighboring nodal values in that direction. The TVD-RK scheme integrates the resulting equations in time to get the point values as a function of time. It is relatively easier to add other dimensions in this method because the spatial derivatives are independent of the coordinate directions. A common behavior of the higher-order polynomials at discontinuities is that they generally introduce oscillatory behavior, and this oscillation increases with the order of the approximation. These oscillations can be eliminated or suppressed by the usage of the essentially nonoscillatory method and the improvement of these WENO methods. They are achieved by systematically adopting or selecting the stencils based on the smoothness of the function, which is being approximated. Although shock-capturing algorithms such as monotonic upstream-centered schemes for conservation laws and ENO are robust, they are locally first-order accurate at the shock [46]. This may introduce oscillations behind the shock wave. One alternative for this problem is to use shock-fitting methods. In this method, the shock waves are treated as a sharp interface. Thus high-order accuracy can be obtained [47] without spurious oscillations. However, in this paper, shock-capturing methods are used because of their robustness. The direct numerical simulation (DNS) solver [27,42,48,49] used in the present study is extensively validated [50] to verify that the spurious oscillations do not exist or are negligible in the calculations.

B. Linear Stability Theory

The basic idea in the linear stability theory is to assume all physical quantities have small disturbances that are a function of space and time. The resultant unsteady equations of motion with the same boundary condition are solved and the solution is investigated in order to determine if they damp, oscillate, or diverge. In the Navier–Stokes equations, physical quantities with mean variables and corresponding disturbances can be shown as

$$\begin{aligned} &u = \bar{U} + \tilde{u}, \quad v = \bar{V} + \tilde{v}, \quad w = \bar{W} + \tilde{w} \\ &p = \bar{P} + \tilde{p}, \quad \tau = \bar{T} + \tilde{T}, \quad \rho = \bar{\rho} + \tilde{\rho} \\ &\mu = \bar{\mu} + \tilde{\mu}, \quad \lambda = \bar{\lambda} + \tilde{\lambda}, \quad k = \bar{k} + \tilde{k} \end{aligned} \tag{20}$$

Because the disturbances are assumed as small, they can be linearized; in other words, the quadratic or higher disturbance terms and their derivatives are neglected as shown:

$$(\tilde{u}, \tilde{v}, \tilde{w}) = [\hat{u}(y), \hat{v}(y), \hat{w}(y)]e^{i(\alpha x + \beta z - \omega t)} \tag{21}$$

$$\tilde{p} = \hat{p}(y)e^{i(\alpha x + \beta z - \omega t)} \tag{22}$$

$$\tilde{T} = \hat{T}(y)e^{i(\alpha x + \beta z - \omega t)} \tag{23}$$

where α and β are the wave numbers in x and z directions, respectively; and ω is the angular frequency. β is only used in the test cases to compare the results with those of Malik [8]. In the rest of the paper (Sec. III), β is taken as zero, which corresponds to the zero-incidence angle disturbance. The Navier–Stokes equations along with the boundary conditions can be represented as a system of ordinary differential equations. The resultant system of equations is given in Ref. [51] along with the details of the system. To solve the resultant system, Malik's finite difference method [8] is followed along with the suggested boundary conditions.

The test cases that are used for the validation of the linear stability code are described in Table 1, where the Mach number, Reynolds number, stagnation temperature, angular frequency, and wave numbers are given. They correspond to various scenarios from incompressible to hypersonic cases to measure the capability of the code in varying flow conditions. It has to be noted that test conditions include both spatial and temporal stability problems.

Table 1 Flow conditions of test cases used to validate the linear stability code[a]

Test case	Mach number	Reynolds number	Total temperature, °R	α	β	ω
1	10^{-6}	580	500	0.179	0	— —
2	0.5	2000	500	0.1	0	— —
3	2.5	3000	600	0.06	0.1	— —
4	10.0	1000	4200	0.12	0	— —
5	4.5	1500	1100	— —	0	0.23

[a]The cases are based on the test cases used in Malik's [8] paper for the accurate comparison.

Table 2 Real and imaginary parts of phase speed c for test case 1; angular frequencies ω for test cases 2, 3, and 4; and wave number α for test case 5

	Present code		Malik's method [8]	
Test case	Real	Imaginary	Real	Imaginary
1	0.3641	0.0079	0.3641	0.0079
2	0.0291	0.0022	0.0291	0.0022
3	0.0367	0.0006	0.0367	0.0006
4	0.1159	0.0002	0.1159	0.0002
5	0.2534	−0.0026	0.2534	−0.0025

The solutions of the test cases are given in Table 2. The first test case results are for the phase speed, which is defined as $c = (\omega/\alpha)$. The last test case is for the spatial stability problem where the result is complex α. The rest of the test cases are for temporal stability problems where the results are complex ω. The results showed great agreement with the provided data. Additionally, the spatial stability code will be validated with the DNS solutions of the Mach 6 flow.

III. Results

Previous research has shown that wall cooling and heating affect the stability of the hypersonic boundary layer. To investigate the effect of local wall cooling, we performed hypersonic steady flow simulations at a freestream Mach number of 6.0 over a 5 deg half-angle cone with a small nose bluntness (0.0254 mm), which was described in the experimental study of Horvath et al. [52]. In their wind-tunnel tests, the unit Reynolds number was 25.59×10^6/m, the freestream temperature was 63.3 K, and the ratio of the adiabatic wall temperature to the freestream temperature was 7.052. The baseline adiabatic flow simulations employed the aforementioned ratio to enforce the adiabatic wall temperature.

After obtaining the adiabatic flow, we applied entire or local wall cooling and studied various cooling strip lengths, locations, and temperature profiles. Table 3 summarizes all the cases considered in this study. Figure 3 shows the cooling profiles for the $0.4 \times T_{\text{ad}}$ case. In the figure, T^* corresponds to the wall to adiabatic wall-temperature ratio. The spatial length is scaled according to the strip location as

$$\frac{x - x_{\text{strip,first}}}{x_{\text{strip,last}}}$$

The flat profile is obtained by forcing every point on the cooling strip to equal the wall temperature given in Table 3. The strip is divided into three equal pieces for the smooth flat case. The first and last pieces are modeled using second-order polynomials, and the middle piece is generated by forcing the wall temperature given in Table 3. The parabolic profile is obtained by a second-order polynomial, and the Gaussian profile is obtained by a Gaussian distribution function.

The baseline case is chosen to validate the accuracy of the steady flow solution. First, we conducted a mesh independence study to verify that the mesh resolution does not affect the numerical solutions. Figure 4 shows the wall pressure distribution for two different

Downloaded by OKLAHOMA STATE UNIVERSITY on October 28, 2022 | http://arc.aiaa.org | DOI: 10.2514/1.A35404

Downloaded by OKLAHOMA STATE UNIVERSITY on October 28, 2022 | http://arc.aiaa.org | DOI: 10.2514/1.A35404

Table 3 Cooling strip and wall-temperature values[a]

Case	Temperature	Cooling location	Cooling profile
1	$1.0 \times T_{ad}$	Baseline	— —
2	$0.6 \times T_{ad}$	Full	— —
3	$0.4 \times T_{ad}$	Full	— —
4	$0.6 \times T_{ad}$	$x = 44.08$–53.49 mm	Flat
5	$0.4 \times T_{ad}$	$x = 44.08$–53.49 mm	Flat
6	$0.6 \times T_{ad}$	$x = 44.08$–53.49 mm	Parabolic
7	$0.4 \times T_{ad}$	$x = 44.08$–53.49 mm	Parabolic
8	$0.6 \times T_{ad}$	$x = 44.08$–53.49 mm	Smooth flat
9	$0.4 \times T_{ad}$	$x = 44.08$–53.49 mm	Smooth flat
10	$0.6 \times T_{ad}$	$x = 44.08$–53.49 mm	Gaussian
11	$0.4 \times T_{ad}$	$x = 44.08$–53.49 mm	Gaussian
12	$0.4 \times T_{ad}$	$x = 44.08$–120.84 mm	Smooth flat
13	$0.4 \times T_{ad}$	$x = 126.21$–202.97 mm	Smooth flat

[a]For the full wall cooling cases, the wall temperature is as given in the table. For the local cooling cases, the cooling strip temperature is as given in the table, and the rest of the wall is adiabatic.

grids where the number of elements in the wall-normal direction is increased 1.7 times for the second grid. An excellent agreement is found between the two grids. In addition, we tested the grids using an unsteady simulation and introduced a sinusoidal disturbance wave

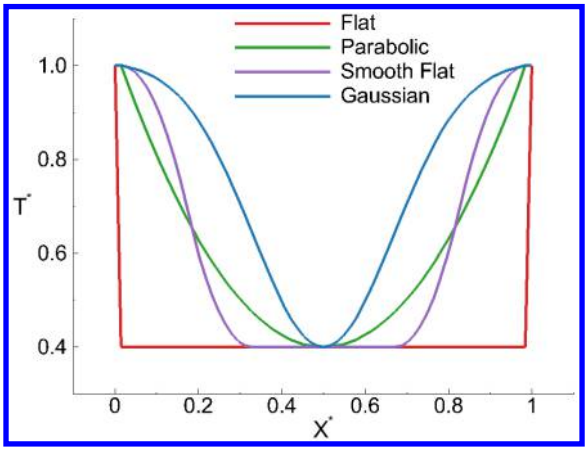

Fig. 3 Profiles of temperature distributions over the cooling strip for $0.4 \times T_{ad}$ case. T^* corresponds to T_w/T_{ad}. X^* corresponds to $(x - x_{strip,first})/x_{strip,last}$.

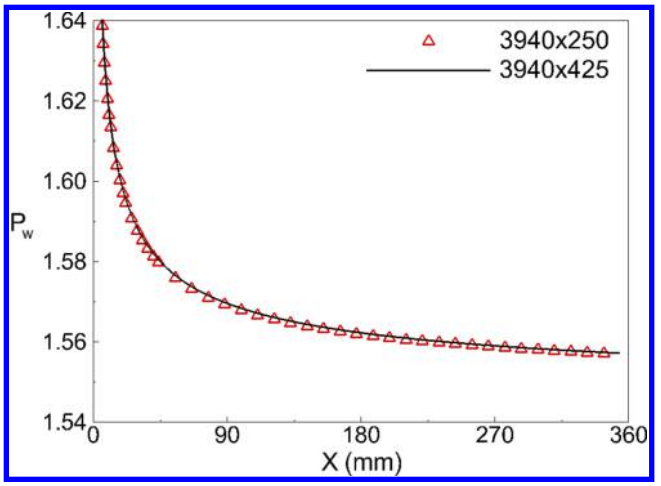

Fig. 4 Wall pressure obtained from steady simulations using two different stretched grids. The second grid includes 1.7 times more elements in the wall-normal direction.

with a frequency of 468 kHz to the flowfield. The unsteady simulations predicted the same wall pressure fluctuations for both grids. As a result, we decided to use the 3940×425 grid setup for the rest of this paper.

Next, we validated the linear stability code with our direct numerical simulation solver [42]. In the DNS, we introduced acoustic disturbances from the inlet boundary at $F = 1.00 \times 10^{-4}$ (390 kHz) and $F = 1.20 \times 10^{-4}$ (468 kHz). To remain in the linear regime, the amplitude of the forcing freestream acoustic waves was given a small value of 1×10^{-5}, which was nondimensionalized by the freestream pressure. The acoustic field is in the form of Eq. (22). Interested readers can refer to Refs. [50,53,54] for details of the disturbance generation and implementation for the DNS. The dimensionless frequency F is

$$F = \frac{2\pi f \nu_\infty}{U_\infty^2} \tag{24}$$

where f is the dimensional frequency; and ν_∞ and U_∞ are the freestream kinematic viscosity and velocity, respectively. The results are compared in Fig. 5, and an excellent agreement is observed. In this figure, the amplitude obtained from the LST is calculated using $A(x) = \exp(N(x, F))$, where $N(x, F)$ is

$$N = \int_{x_0}^{x} \sigma^*(x, F)\, \mathrm{d}x \tag{25}$$

Here, σ is defined as $-\alpha_i$, and σ^* is the scaled growth rate. For the scaling of the growth rate, the Blasius length ($\sqrt{\nu_e x/U_e}$) is used, where x is a dimensional spatial location rather than a constant. The dimension of x is in millimeters. Thus, the dimension of the growth rate is one per millimeter. The integrations for N factors are done accordingly. Figure 5 shows that our linear stability code accurately captures the unstable wave growth rate for both frequencies. In Fig. 5, the physical coordinate system (x, y) is used in the governing equations, and the computational curvilinear coordinate system (ξ, η) is used in the numerical calculations. The flow parameters used in the simulations presented in this paper are based on the cone experiments conducted at NASA Langley Research Center's Mach 6 wind tunnels by Horvath et al. [52].

A. Validation of Steady Flow

The steady flow is solved until it converges to machine zero (10^{-11}). Figure 6 illustrates the Mach contour plot around the nose region and the entire computational domain. First, the shock angle calculated from the steady flow data is compared with the Taylor–Maccoll solution [55]. Both the mean flow and the Taylor–Maccoll solution provided the same value of 10.64 deg. We should note that the nose radius in this study is 0.0254 mm, and therefore the oblique shock angle converges to the inviscid limit. In addition, for such a small nose bluntness, the stabilization effect of the entropy layer is negligible [42,56,57].

Additionally, we compared the steady flow velocity and temperature profiles with similarity solutions in Fig. 7 and found an excellent agreement. Here, the similarity parameter η is

$$\eta = \frac{y_n}{\sqrt{\nu_e s/U_e}} \tag{26}$$

where y_n is the wall-normal distance; s is the distance along the surface of the cone; and ν_e and U_e are the kinematic viscosity and the velocity, respectively, at the boundary-layer edge. The velocity and temperature are nondimensionalized with the corresponding edge values.

B. Stability Analysis of Full Cooling

Previous studies showed that wall cooling has a stabilizing effect on the first mode, whereas it destabilizes the second mode. To compare the full cooling with the local cooling, the full cooling cases

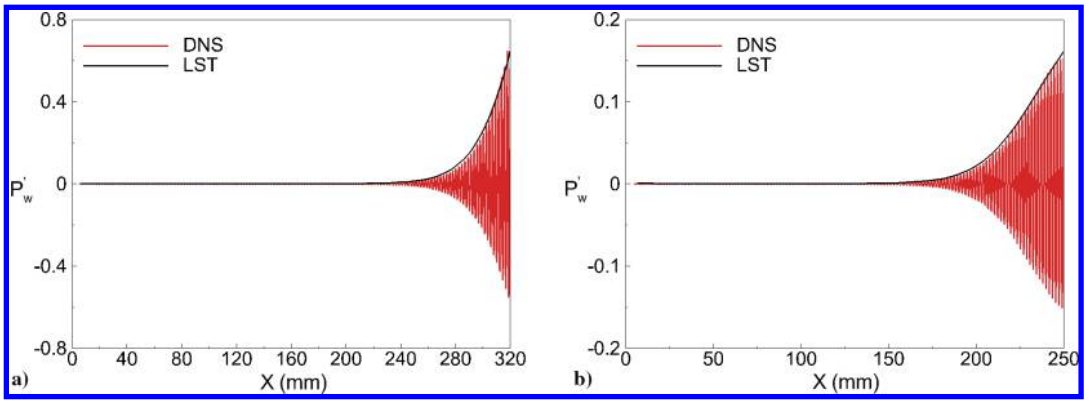

Fig. 5 Comparison of wall pressure fluctuation results obtained from DNS code and linear stability code for dimensionless frequencies a) $F = 1.00 \times 10^{-4}$ and b) $F = 1.20 \times 10^{-4}$. The linear stability code captured growth rates accurately.

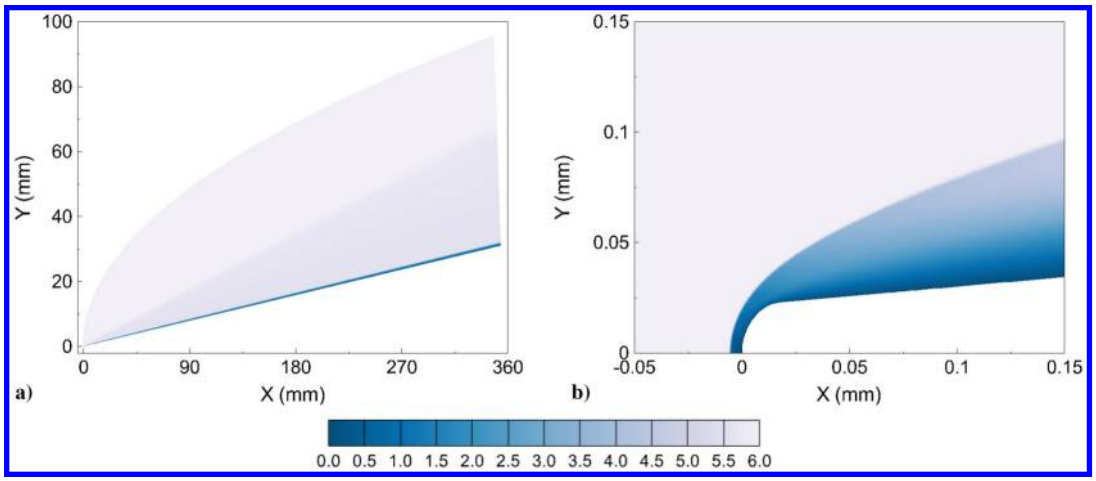

Fig. 6 Distribution of Mach number a) in full computation domain and b) around nose region. The computational domain includes 3940 elements in the axial direction and 425 elements in the wall-normal direction.

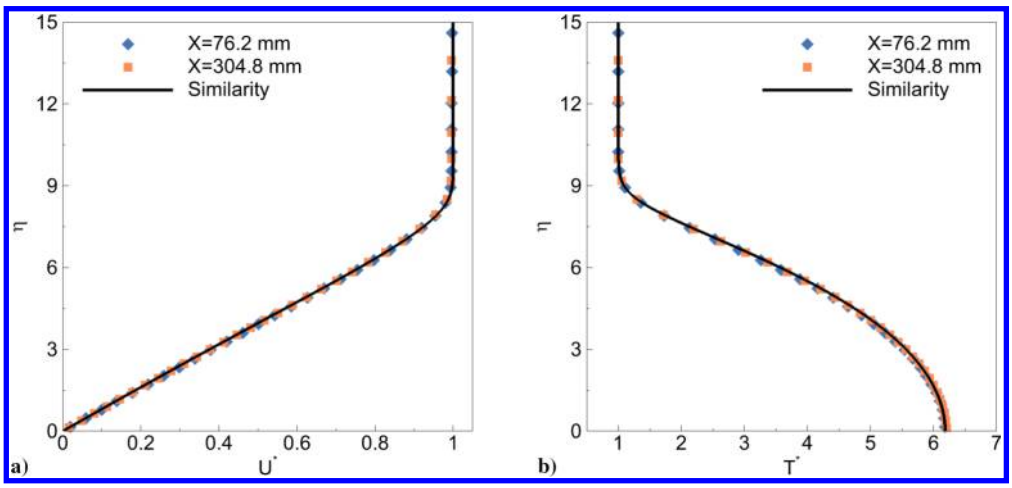

Fig. 7 Validation of normalized a) velocity and b) temperature distribution within boundary layer with similarity solution obtained for $M = 6$ flow with freestream temperature of 63.3 K. Normalization is done with corresponding edge values.

given in Table 3 are solved with the high-order, axisymmetric, and steady Navier–Stokes solver. The resultant steady flow is used in the predictions of the growth rates and amplifications of unstable disturbances by the linear stability code. First, the wall pressure and normalized boundary-layer thickness are plotted as a function of spatial distance in Fig. 8. The boundary-layer thickness is scaled with the maximum boundary-layer thickness of the baseline case. The wall pressure is high in the nose region and reaches a constant value as the air moves downstream. The wall cooling leads to lower wall pressure than the baseline case. The boundary-layer thickness decreases with the wall cooling as well. At the end of the domain, the boundary-layer thickness of the $0.6 \times T_{ad}$ and $0.4 \times T_{ad}$ cases are 0.79 and 0.69 times lower than the baseline case, respectively.

The phase speed of the mode F and mode S disturbance waves are given in Fig. 9a. Mode F originates from the fast acoustic spectrum, whereas mode S originates from the slow acoustic spectrum [58]. For the baseline case with the dimensionless frequency of $F = 1.3 \times 10^{-4}$, the two modes synchronize at the downstream location of $x = 165.822$ mm. In passive hypersonic boundary-layer control methods, such as roughness and porous wall usage, the

Downloaded by OKLAHOMA STATE UNIVERSITY on October 28, 2022 | http://arc.aiaa.org | DOI: 10.2514/1.A35404

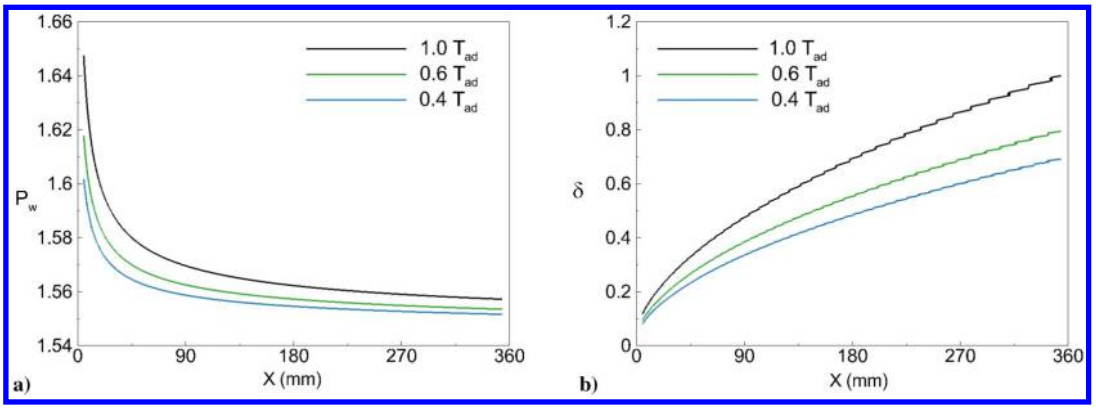

Fig. 8 Distribution of a) wall pressure and b) boundary-layer thickness of steady solution for the full wall cooling cases given in Table 3. Boundary-layer thickness is scaled with maximum boundary-layer thickness of baseline case.

Downloaded by OKLAHOMA STATE UNIVERSITY on October 28, 2022 | http://arc.aiaa.org | DOI: 10.2514/1.A35404

location of the synchronization point is crucial. Fong et al. [59,60] showed that it is efficient to use the roughness element downstream of the synchronization point in order to damp the disturbances. When the roughness element is placed upstream of the synchronization point, the disturbances are amplified. Moreover, Wang and Zhong [61,62] stated the importance of the synchronization point for the porous coating. Their studies showed that porous coating can be effective when it is placed downstream of the synchronization point. The full wall cooling slows down the mode F phase speed decrements, and the synchronization occurs further downstream than the baseline case. The locations of the synchronization points are $x = 206.159$ mm and $x = 267.336$ mm for the $0.6 \times T_{ad}$ and $0.4 \times T_{ad}$ cases, respectively.

The growth rate of the slow acoustic wave is given in Fig. 9b. The growth rate becomes positive, and disturbances start to grow at $x = 73.495$ mm for the baseline case. For the full wall cooling cases, the growth rate decreases until the phase speeds of mode F and mode S are close. Once the phase speeds of mode F and mode S are close enough, the growth rate starts to increase and crosses the positive side where disturbances are amplified. The slope of the growth rate increases with the lower wall temperatures. Additionally, the maximum growth rate reached 1.52 and 1.78 times higher values than the baseline case for the $0.6 \times T_{ad}$ and $0.4 \times T_{ad}$ cases, respectively. Although the growth rate is increasing and reaching higher values than the baseline case, the maximum growth rate location moves downstream because of the initial stabilization of the disturbances. This trend was observed in the previous DNS study of Kara et al. [27].

The downstream growth of instability is characterized by the N factors, which are computed at various dimensionless frequencies. The transition onset point can be estimated from the N-factor diagram by defining an empirical constant that corresponds to the transition N value, N_{tr}. The location that reaches the empirical N_{tr} point the first time can be predicted as the transition onset location. Figure 10 shows

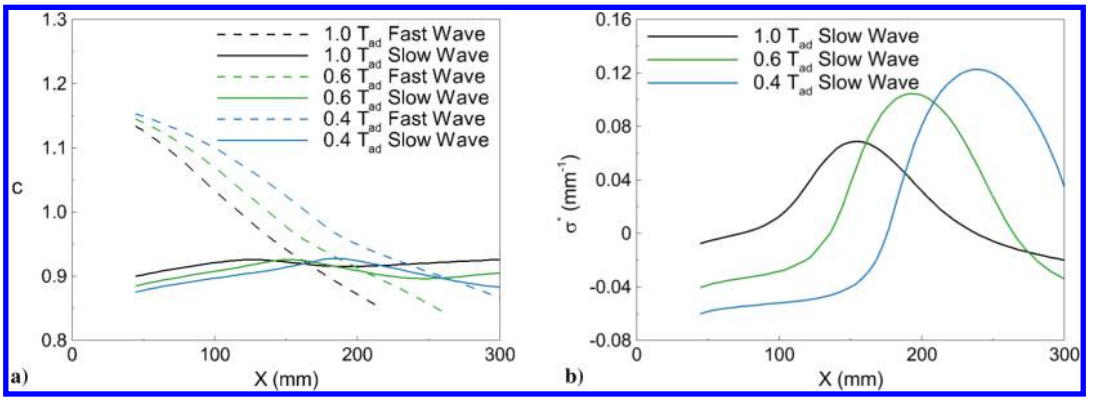

Fig. 9 Spatial linear stability results of full wall cooling cases: a) phase speed c of fast and slow waves, and b) growth rate of slow wave for cases given in Table 3. Dimensionless frequency is taken as $F = 1.3 \times 10^{-4}$.

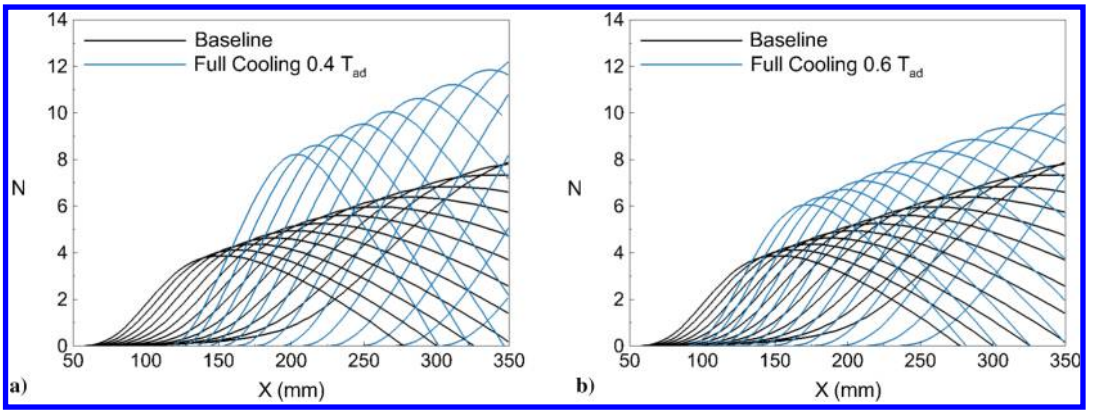

Fig. 10 N-factor diagrams of full wall cooling with a) $0.4 \times T_{ad}$ and b) $0.6 \times T_{ad}$ cases. Dimensionless frequency range is between $F = 1.0 \times 10^{-4}$ and $F = 1.6 \times 10^{-4}$, which correspond 390–625 kHz.

the N factors in the dimensionless frequency range from $F = 1.00 \times 10^{-4}$ to $F = 1.60 \times 10^{-4}$, which corresponds to the range of 390–625 kHz. In this plot, the N factors are calculated by starting from the neutral point $x_0 = x_n$. The increased growth rates of the full wall cooling led to higher N factors than the baseline case. For a constant frequency, full wall cooling reached 2.14 and 1.57 times higher N values for the $0.4 \times T_{ad}$ and $0.6 \times T_{ad}$ cases, respectively. The increase in the growth rate and the N factors agree with the previous findings [27,63].

C. Effect of Local Cooling with a Short Strip

After the full cooling cases, a short cooling strip is placed on the surface in between $x = 44.08$ mm and $x = 53.49$ mm. The wall temperatures for the short strip cases are given in Table 3. For each temperature case, four different cooling profiles are studied. The cooling profiles are given in Fig. 3. The local wall cooling leads to a temperature drop near the upstream boundary of the cooling strip. The sudden temperature drop decreases the boundary-layer thickness and the temperature; therefore, expansion waves occur at the leading edge of the cooling strip. Around the downstream boundary of the cooling strip, the wall temperature rises significantly and the boundary-layer thickness increases. These cause compression waves around the trailing edge of the cooling strip. Figure 11 shows the pressure contours of the two different wall temperatures with the flat profile. The expansion (white region) and compression (dark blue region) waves around the cooling strip are quite noticeable for the $0.4 \times T_{ad}$ case (Fig. 11a).

Figure 12 shows the wall pressure distribution around the cooling strip for varying temperatures and cooling profiles. In the rest of the computational domain, the wall pressure is identical to the baseline (adiabatic) case, and so only the region around the cooling strip is

Downloaded by OKLAHOMA STATE UNIVERSITY on October 28, 2022 | http://arc.aiaa.org | DOI: 10.2514/1.A35404

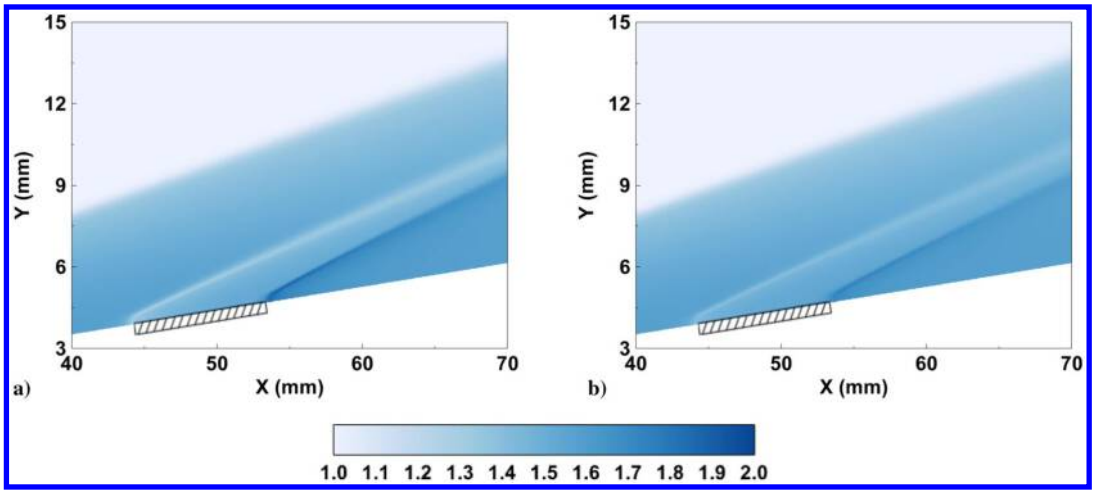

Fig. 11 Variation of dimensionless pressure around cooling strip with flat cooling profile and boundary conditions for cooling strip: a) $0.4 \times T_{ad}$ and b) $0.6 \times T_{ad}$. Cooling strip locations are shown with a dashed box. Pressure is normalized with the freestream pressure value.

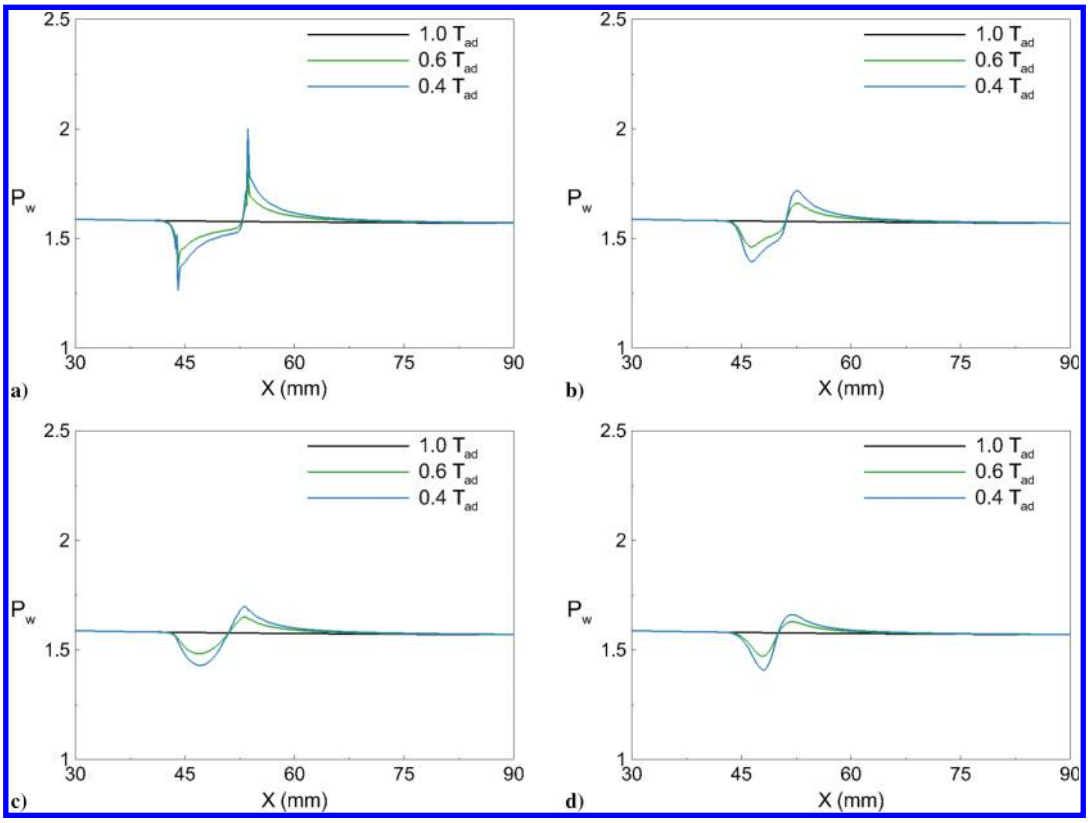

Fig. 12 Wall pressure distribution of local cooling cases with a short strip, given in Table 3 for a) flat profile, b) smooth flat profile, c) parabolic profile, and d) Gaussian profile.

Downloaded by OKLAHOMA STATE UNIVERSITY on October 28, 2022 | http://arc.aiaa.org | DOI: 10.2514/1.A35404

provided. The wall cooling has a small upstream influence on the steady flow. However, there is a strong downstream influence. The downstream effect starts after the cooling strip, and it is carried over approximately two strip lengths. After the downstream effect, the wall pressure reaches the undisturbed value, which corresponds to the wall pressure distribution of the baseline case. The wall pressure distribution over the cooling strip is highly affected by the cooling profile. Although the wall pressure distributions of the parabolic and Gaussian profiles are similar to the cooling profile (Figs. 12c and 12d), the flat and smooth flat cooling profiles lead to a profile starting with a high gradient and decreasing in the spatial distance (Figs. 12a and 12b). Even though the wall pressure distributions over the cooling strips are different for each cooling profile, the downstream effect is similar for all profiles except the magnitude.

The negative temperature gradient in the axial direction on the wall decreased the wall pressure drastically; in other words, when the temperature gradient is zero, the wall-temperature profile is flat. The wall pressure tends to increase slowly. Once the wall-temperature gradient is positive, the wall pressure increases drastically to the maximum point. After that point, pressure recovery starts. Figure 13 illustrates the change in the wall pressure with the wall temperature for the $0.4 \times T_{ad}$ case with the smooth flat cooling profile. For the flat profile, there is a sharp decrease in the wall pressure around the upstream area of the cooling strip. Other profiles do not have this sharp decrease. This behavior was observed in Zhao et al.'s paper [37]. The strong expansion wave forming upstream of the cooling strip may lead to such a high gradient.

The growth rates of the local cooling cases with a short strip for a dimensionless frequency of $F = 1.3 \times 10^{-4}$ are illustrated in Fig. 14. In the upstream region, until the cooling strip, there is not any effect caused by the cooling strip; therefore, the growth rates coincide with the baseline case. Over the cooling strip, the growth rate starts to decrease. The decrease is directly related to the cooling profile. The flat cooling profile led to the highest growth rate reduction, whereas the Gaussian cooling profile led to the lowest. In the downstream boundary of the cooling strip, the growth rate starts to increase; and it reaches the baseline growth rate after approximately two strip lengths. The growth rate increase is similar to pressure recovery. The growth rate of the local cooling remains higher than the baseline case for the rest of the computational domain. The maximum growth rate is related to the maximum cooling introduced to the system. The maximum cooling among all profiles is introduced with the flat cooling profile, which led to the highest growth rate. The lowest cooling is introduced with the Gaussian profile, which has the minimum peak growth rate within the local cooling cases. One interesting observation from the growth rate plots is that parabolic and smooth flat profiles led to the same growth rate change for both of the cases. This shows that the total introduced cooling is more effective than the cooling profile. Another interesting observation is that the wall temperature is less effective on the growth rate. Figure 15 shows the $0.6 \times T_{ad}$ flat profile case and the $0.4 \times T_{ad}$ smooth flat profile case. The growth rate distributions coincide with each other, except for the small difference in the leading edge and the trailing edge of the cooling strip. However, these small differences can be negligible for the N factors.

The conventional e^N method [64] assumes that all unstable waves are available over the surface. The lower limit of the integration given in Eq. (25) starts from the lower neutral branch. This assumption provides reliable results for the adiabatic test cases. However, local cooling has a damping effect on the disturbances before the neutral point. Thus, the growth rate decreases because of the local cooling strip (Fig. 14). If the integration starts from a neutral point, the damping effect will be omitted and the N factors will be misleading. Because the freestream values are almost same for both local cooling and adiabatic cases up to a location close to the cooling strip, amplitudes of the unstable wave are the same at that location for local cooling and adiabatic cases [35]. This allows us to calculate the N factors starting from a constant point [65]. To further illustrate the statement, second-mode waves of all frequencies entering the boundary layer will be excited; and the receptivity process will be completed by a constant station. It has to be noted that the freestream values are identical. Thus, the initial amplitude of the unstable waves is approximately the same for all frequencies at that constant location. With these assumptions, the N factors can be calculated from that constant point to include the initial damping coming from local cooling [35]. It is important to state that initial damping in the adiabatic (baseline) case is weak. However, in the local cooling case, there may be substantial damping. Now, the question is the location of the starting point of the integral. We defined the location of the starting point as $x_0 = 6.69$ mm. The selection of the starting point is defined by the point where the initial amplitude of the disturbances is almost identical for different frequencies. In other words, the aforementioned location of the receptivity process is completed. To visually illustrate the idea, the N factors will be calculated from $x_0 = 6.69$ mm and $x_0 = x_n$ to show the discrepancy between DNS and

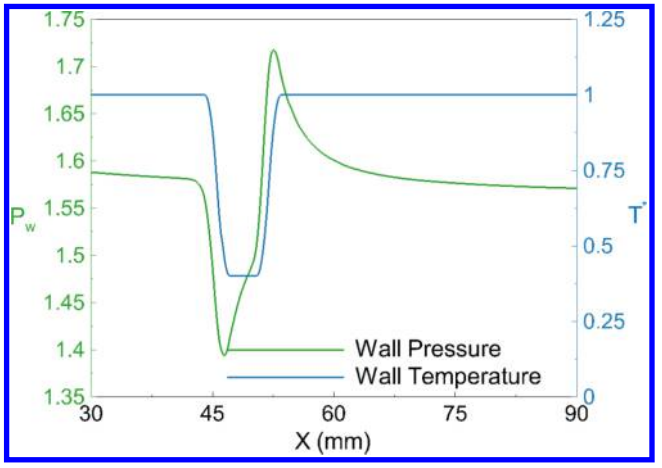

Fig. 13 Distribution of wall pressure and wall temperature over cooling strip for $0.4 \times T_{ad}$ case with smooth flat cooling profile.

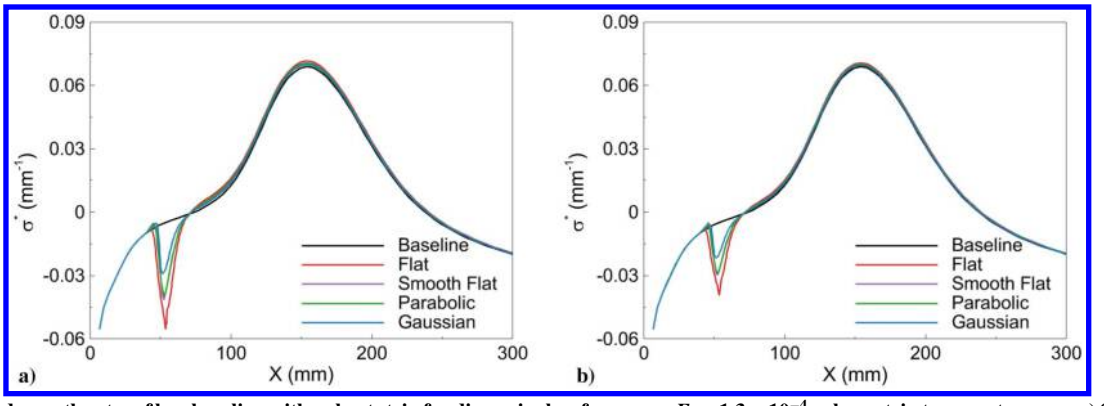

Fig. 14 Scaled growth rates of local cooling with a short strip for dimensionless frequency $F = 1.3 \times 10^{-4}$, where strip temperatures are a) $0.4 \times T_{ad}$ and b) $0.6 \times T_{ad}$. Growth rate is scaled with the Blasius length.

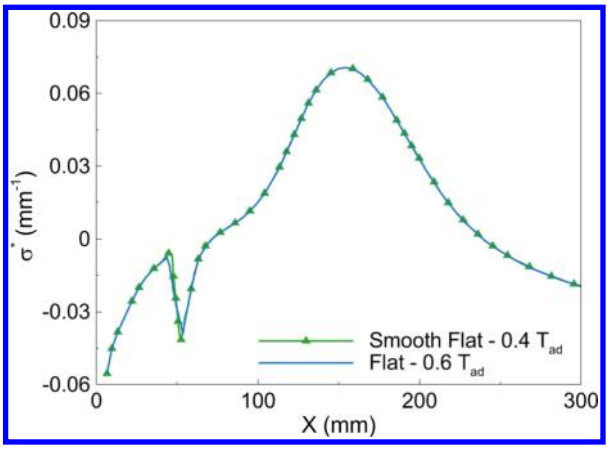

Fig. 15 Scaled growth rates of local cooling with a short strip for $0.6 \times T_{ad}$ flat profile case and $0.4 \times T_{ad}$ smooth flat profile case, where the dimensionless frequency is $F = 1.3 \times 10^{-4}$.

LST. However, in the short strip case, the amplitudes of local cooling and the baseline cases are so close to each other. Thus, we postpone the illustration of the assumption to the next subsection (Sec. III.D) for a more emphasized illustration. In this subsection, the N factors will be calculated from $x_0 = 6.69$ mm. To evaluate the idea and verify that LST provides accurate results for local cooling cases, we performed a DNS and introduced disturbances from the inlet with a frequency of $F = 1.3 \times 10^{-4}$ and an amplitude of 1×10^{-5} for the baseline and cooling cases; the rest of the properties of the disturbance are identical to the one used in LST validation (Fig. 5). We compared the DNS and LST results and observed an excellent agreement, as shown in Fig. 16. The figure illustrates that the growth rate of the instabilities is captured with great accuracy in the region of $x > 100$ mm. However, LST overpredicted the wall pressure upstream of this region. The discrepancy between LST and DNS is due to nonparallel flow near the nose region. Other researchers [37,50,48,66] also observed a similar phenomenon. Additionally, it has to be noted that the initial amplitudes of LST solutions are arbitrary because the receptivity is not considered [35]. In the following subsection, we will compare the results from LST and DNS for different cooling strip lengths.

The N factors are calculated from the growth rate for the dimensionless frequency range from $F = 1.0 \times 10^{-4}$ to $F = 1.4 \times 10^{-4}$, which corresponds to 390–546 kHz. Figure 17 shows the N factors for the $0.4 \times T_{ad}$ case for flat, smooth flat, and Gaussian profiles. The parabolic profile is not included because the N-factor diagrams were identical to the smooth flat results. The results given in Fig. 17 show that the local cooling with a short strip has a small stabilizing effect on the N-factor diagrams. The difference between flat cooling and the baseline case is slightly more distinguishable than the others (Fig. 17a). However, the Gaussian profile's N-factor plots almost coincide with the baseline case (Fig. 17c).

D. Effect of Local Cooling with a Long Strip

The local cooling with a short strip showed that the disturbances can be damped with a local cooling. However, damping was small for the short strip. In this subsection, the first point of the strip kept was constant and the length of the strip extended to 120.28 mm. For comparison purposes, simulations with the extended strip are limited to the smooth flat profile, which gives slightly higher stabilization than the Gaussian profile and slightly less stabilization than the flat profile. It has to be noted that the smooth flat profile growth rate development and the N-factor diagrams were identical to the parabolic profile.

Initially, the growth rate of the extended strip was calculated. Figure 18 shows the growth rate of the baseline case of local cooling with a short strip and a long strip, where the wall temperature on the strip is $0.4 \times T_{ad}$ and the dimensionless frequency is $F = 1.3 \times 10^{-4}$. The longer strip led to higher stabilization than the short strip over the cooling region. In the short strip case, the decrease in the growth rate lasts over the entire strip length. However, for the long strip case, the

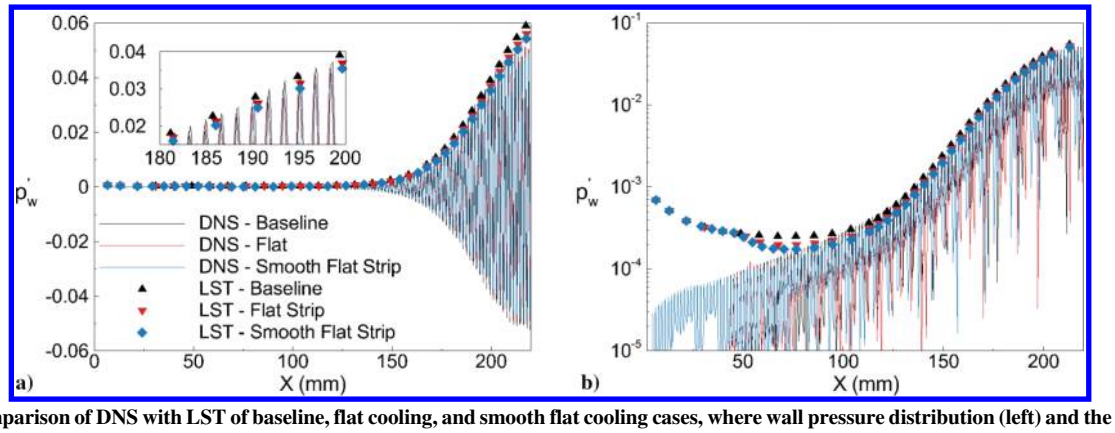

Fig. 16 Comparison of DNS with LST of baseline, flat cooling, and smooth flat cooling cases, where wall pressure distribution (left) and the same plot in the logarithmic axis (right) are given. Both figures share the same legend. The location of the cooling strips is in the range $x = 44.08$–53.49 mm.

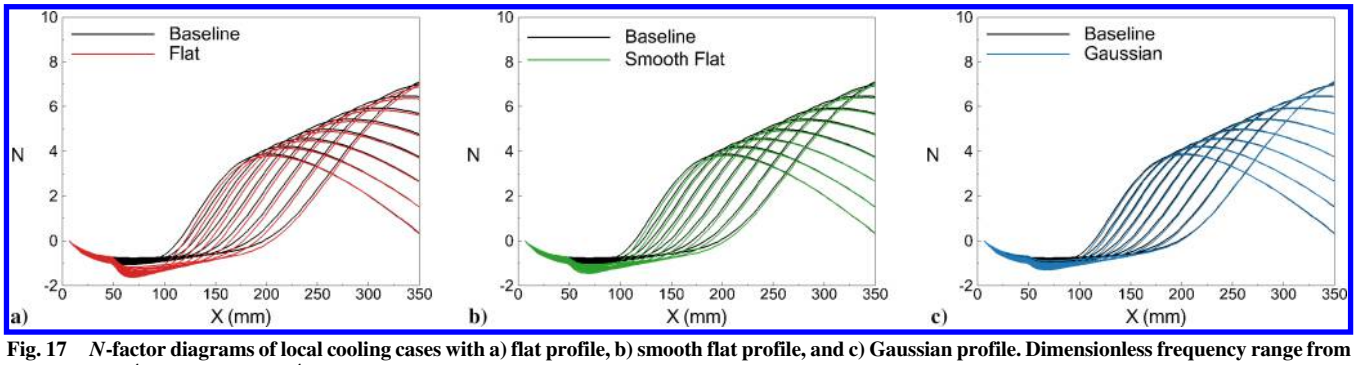

Fig. 17 N-factor diagrams of local cooling cases with a) flat profile, b) smooth flat profile, and c) Gaussian profile. Dimensionless frequency range from $F = 1.0 \times 10^{-4}$ to $F = 1.4 \times 10^{-4}$.

Downloaded by OKLAHOMA STATE UNIVERSITY on October 28, 2022 | http://arc.aiaa.org | DOI: 10.2514/1.A35404

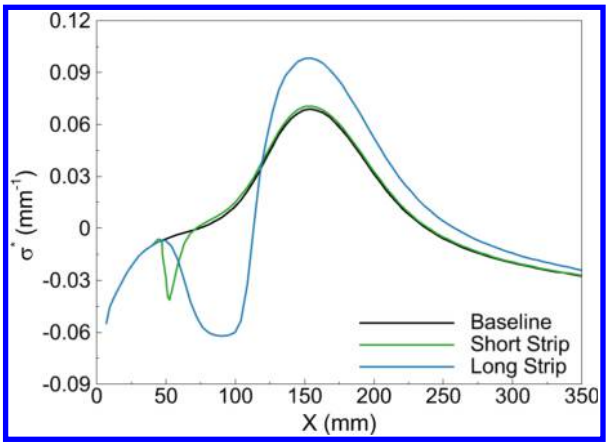

Fig. 18 Scaled growth rate comparison of baseline, short strip, and long strip cases, with strip temperature of $0.4 \times T_{ad}$. Dimensionless frequency is taken as $F = 1.3 \times 10^{-4}$.

growth rate started to increase at $x = 90.38$ mm. This point is close to where the wall temperature is rising due to the cooling profile. The increase in the wall temperature led to an increase in the wall pressure. Moreover, the growth rate started to increase with the pressure and temperature. Another reason for the high increase in the growth rate is the synchronization point. The energy transfer between fast and slow acoustic waves leads to an increase in the growth rate for the slow acoustic wave because the fast acoustic wave transfers energy to the slow acoustic wave. Eventually, the maximum growth rate increases drastically for the long strip with the help of pressure recovery. Additionally, the growth rate remains higher than the baseline case for the rest of the computational domain.

The disturbance wave is initially damped by the cooling strip; however, the maximum growth rate is 1.43 times higher than the baseline maximum growth rate. The overall stabilization/destabilization effect can be observed from the N factors. However, first, to evaluate the accuracy of LST with the long strip, we will present the validation of LST using DNS results for different cooling strip lengths. It has to be noted that the N factor used in amplitude estimation for LST is calculated from the constant location. We performed the DNSs for cases 1, 9, and 12, given in Table 3 using a nondimensional disturbance frequency of $F = 1.3 \times 10^{-4}$. Figure 19 shows the comparison of the LST and DNS results for the baseline, short strip, and long strip cooling cases. The properties of the disturbance are identical to the ones used in LST validation (Fig. 5), except the frequency of the disturbance. We scaled the LST result to match the DNS result for the baseline case at the maximum wall pressure location, and we used the same scaling factor for the local cooling cases. The results show an excellent agreement after $x = 100$ mm for the short strip and baseline cases, as observed in Fig. 16. However, for the long strip case, the location where the LST and DNS results match moved further downstream to $x = 140$ mm. The reason for the increased length is the nonparallel effects over the cooling strip. We conclude that LST provides a reasonable estimate after the longer cooling strip, which ends at 120.28 mm. Thus, the N factors calculated from the LST analysis provide a comparative estimation to understand the cooling strip's effect as compared with the baseline case.

Initially, the N factors are calculated starting from a neutral point [$x_0 = x_n$ in Eq. (25)] for both the baseline (adiabatic) and long cooling strip cases. The dimensionless frequency range is in between $F = 1.00 \times 10^{-4}$ and $F = 1.40 \times 10^{-4}$. The corresponding dimensional frequencies are between 390 and 546 kHz. The results are given in Fig. 20a. N-factor diagrams show that local cooling destabilized the flow. In other words, higher N values are reached by local cooling for every frequency within the test cases. However, DNS results (Fig. 19) show that the pressure perturbations on the wall are

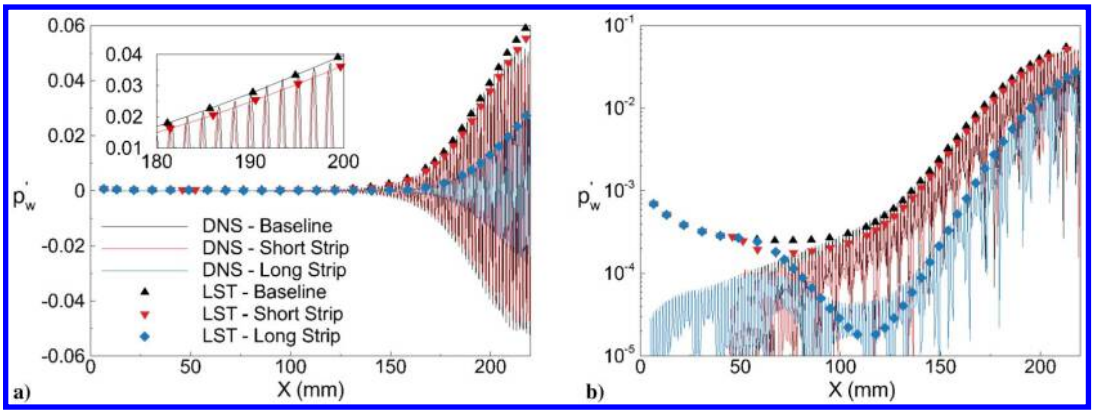

Fig. 19 Comparison of DNS with LST for baseline, short strip, and long strip cooling cases, where wall pressure distribution (left) and the same plot in the logarithmic axis (right) are given. Location of the short cooling strip is in the range $x = 44.08$–53.49 mm, whereas the location of the long strip is in the range $x = 44.08$–120.84 mm.

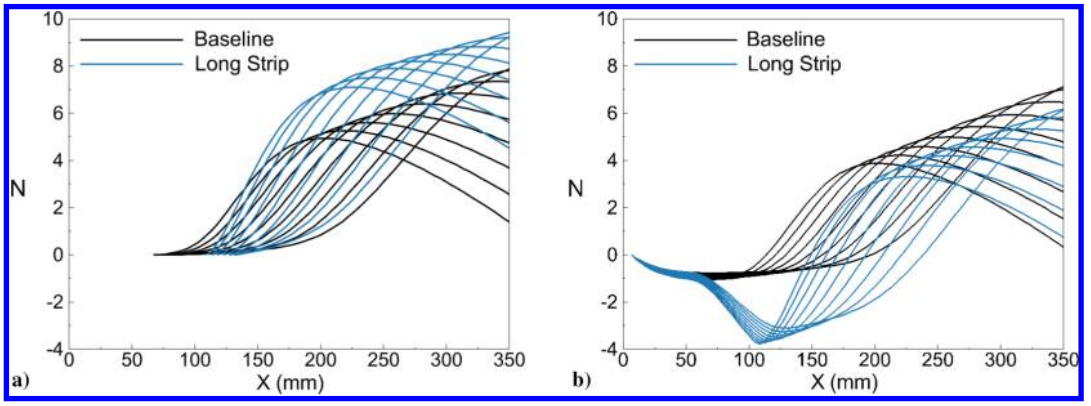

Fig. 20 N-factor diagrams calculated from a) neutral point ($x_0 = x_n$), and b) the constant point ($x_0 = 6.69$ mm). Cases are baseline and local cooling with a long strip, where wall cooling is $0.4 \times T_{ad}$ and the cooling profile is smooth flat.

Downloaded by OKLAHOMA STATE UNIVERSITY on October 28, 2022 | http://arc.aiaa.org | DOI: 10.2514/1.A35404

Downloaded by OKLAHOMA STATE UNIVERSITY on October 28, 2022 | http://arc.aiaa.org | DOI: 10.2514/1.A35404

significantly reduced by the local cooling. The discrepancy between the N factors and DNS is due to the damping effect between $x_0 = 6.69$ mm and $x_0 = x_n$. Because of the aforementioned reasons and assumptions (in Sec. III.C), calculating the N factors from a constant point ($x_0 = 6.69$ mm) will lead to better accuracy when the results are compared with the DNS.

Figure 20b gives the N-factor diagrams of the baseline case and the local cooling with a long strip for the dimensionless frequencies from $F = 1.00 \times 10^{-4}$ to $F = 1.40 \times 10^{-4}$. The corresponding dimensional frequencies are in between 390 and 546 kHz. However, this time, the N factors are calculated from $x_0 = 6.69$ mm instead of $x_0 = x_n$. The N factors show that local cooling with a longer strip decreases the N values 0.86 times when compared with the baseline case. The results showed that the strip length is a parameter for the disturbance wave damping. A short strip slightly stabilized the boundary layer (Fig. 17); however, a longer strip highly stabilized the boundary layer. The limit for the stabilization is the synchronization point. In all of the aforementioned cases, the cooling strip is located upstream of the synchronization points for each of the considered frequencies. The synchronization point is crucial in hypersonic boundary-layer transition. To investigate the effect of the synchronization point, the cooling strip will be placed downstream of the synchronization point.

E. Effect of Synchronization Point

The synchronization point is crucial in passive hypersonic boundary-layer transition control methods. In the hypersonic boundary layer, generally speaking, the fast mode transfers energy to the slow mode, and the slow acoustic disturbances grow. A passive boundary-layer transition control method may severely contribute to this process by decreasing or increasing the amplitude growth. One example for this phenomenon is the location of the roughness element relative to the synchronization point. To damp the disturbance waves, the roughness element has to be located downstream of the synchronization point. Otherwise, it amplifies the disturbances. To investigate the effect of the location of the cooling strip relative to the synchronization point, the cooling strip is placed further downstream at $x = 126.21$–202.97 mm. The synchronization point tends to move upstream with increasing frequency. The new location of the cooling strip will guarantee that synchronization points of a wider frequency range will be upstream of the cooling strip. Figure 21 shows the growth rate of the baseline along with the local cooling from $x = 44.08$ mm to $x = 120.84$ mm and $x = 126.21$ mm to $x = 202.97$ mm. Both of the cooling strips use the smooth flat profile, and the wall temperature on the cooling strip is $0.4 \times T_{ad}$. The dimensionless frequency is $F = 1.60 \times 10^{-4}$. For the baseline case, the amplitude of the disturbance wave decreases until $x = 53.6$ mm. After this point, the growth rate crosses to the positive side, and the amplitude of the disturbances starts to increase. The growth rate

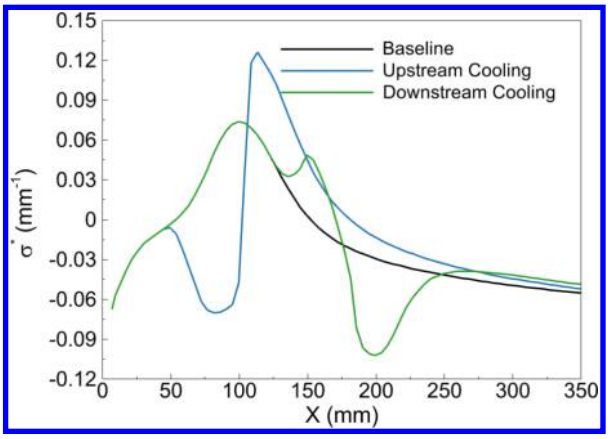

Fig. 21 Growth rates of baseline, local cooling from upstream of synchronization point, and local cooling from downstream of the synchronization point cases. The dimensionless frequency is 1.60×10^{-4}, and the temperature of the cooling strip is $0.4 \times T_{ad}$.

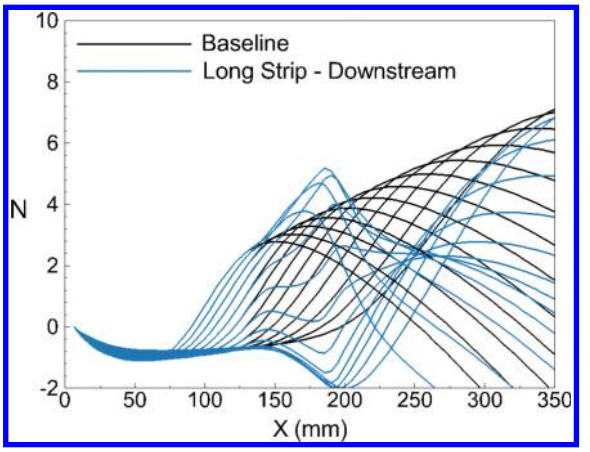

Fig. 22 N factors of local cooling placed in between $x = 126.21$ mm and $x = 202.97$ mm. The dimensionless frequency range is from 1.00×10^{-4} to 1.60×10^{-4}. The temperature of the cooling strip is $0.4 \times T_{ad}$.

increases until $x = 99.2$ mm with the help of the energy transfer from the fast acoustic wave. For the baseline case, the synchronization point is calculated as $x = 111.09$ mm. The cooling strip placed in between $x = 44.08$ mm and $x = 120.84$ mm damps the amplitude of the disturbances. The growth rate crosses the positive side at $x = 102.1$ mm for the strip at $x = 44.08$–120.84 mm. However, the maximum growth rate location is shifted downstream, and the magnitude of it is 1.72 times higher than the baseline case. Once the growth rate reaches the maximum point, it starts to decrease. On the other hand, when the cooling strip is placed downstream of the synchronization point, the growth rate increases up to the peak point of the baseline case. Additionally, the damping effect is reversed in this case, and the local cooling initially amplified the disturbances; after that, it started to damp. Because the growth rate is amplified in the positive region, the amplitudes of the disturbances are further increased by the cooling strip. This behavior is a completely reversed version of the other cases investigated in this paper.

The effect of the location of the cooling strip with respect to the synchronization point can be seen from the N-factor diagram. Figure 22 shows the N-factor diagrams of the local cooling of case 13, given in Table 3 in the dimensionless frequency range from 1.00×10^{-4} to 1.60×10^{-4}. The corresponding dimensional frequencies are in between 390 kHz and 625 kHz. The local cooling increases the N factors up to 1.5 times in the range of 1.45×10^{-4} to 1.60×10^{-4}. In this frequency range, the synchronization point is located upstream; as a result, the effect of the local cooling is reversed, as is shown in Fig. 21. As the frequency decreases, the synchronization point moves downstream. Once the synchronization point appears downstream of the cooling strip, the N factors remain lower than the baseline case.

IV. Conclusions

Full and local cooling are applied to a 5 deg half-angle blunt cone with a 0.0254 mm nose radius to investigate the boundary-layer stabilization of the wall cooling. The steady flow of hypersonic boundary layers is numerically investigated at a freestream Mach number of 6.0 and at a Reynolds number of 25.59×10^6/m. The steady solution is obtained by solving compressible Navier–Stokes equations using the fifth-order-accurate WENO scheme for spatial discretization and a third-order TVD Runge–Kutta scheme for time integration. The growth rates, phase speeds, and N-factor diagrams are calculated with a linear stability code. The computations are initially performed for the adiabatic case, which is used as the baseline case. Then, full wall cooling is introduced to the computational domain with two different wall temperatures: $0.6 \times T_{ad}$ and $0.4 \times T_{ad}$. The linear stability analysis of the full wall cooling for the dimensionless frequency of 1.3×10^{-4} shows that the synchronization point moves downstream 40.3 and 101.5 mm, and the maximum growth rate approximately increases 1.52 and 1.78 times

Downloaded by OKLAHOMA STATE UNIVERSITY on October 28, 2022 | http://arc.aiaa.org | DOI: 10.2514/1.A35404

as compared to the baseline case for the $0.6 \times T_{ad}$ and $0.4 \times T_{ad}$ cases, respectively. The resultant N-factor diagrams of the full wall cooling illustrate that the maximum N values of full wall cooling are 2.14 and 1.57 times higher than the baseline case for each corresponding frequency for the wall temperatures of $0.6 \times T_{ad}$ and $0.4 \times T_{ad}$, respectively. To compare the local cooling and full cooling, a cooling strip is introduced in between $x = 44.08$ mm and $x = 53.49$ mm, and the adiabatic boundary condition is used for the rest of the wall. Four different cooling profiles are used with the cooling strip temperatures of $0.6 \times T_{ad}$ and $0.4 \times T_{ad}$. The profiles used in the simulations are the flat, smooth flat, parabolic, and Gaussian profiles. The results show that the parabolic profile and the smooth flat profile lead to the same growth rate distribution. Additionally, the smooth flat profile with the $0.4 \times T_{ad}$ case and the flat profile with the $0.6 \times T_{ad}$ case lead to the same growth rate distribution. The almost identical growth rate profiles with different temperatures and profiles show that total cooling is a more important parameter than the wall temperature and profile. This phenomenon will be addressed in the future works in detail. On the other hand, the local cooling slightly stabilizes the boundary layer. However, the stabilization is negligible for the short strip (x44.08–53.49 mm). To investigate the length effect, a longer strip is introduced to the computational domain in between $x = 44.08$ mm and $x = 120.84$ mm for the $0.4 \times T_{ad}$ case with the smooth flat profile. Although the maximum growth rate for the long strip increased 1.43 times more than the baseline and short strip cases, the initial stabilization is higher than the short strip. Therefore, the maximum N-factor value of the long strip decreases 0.86 times more than the baseline case. Lastly, the new cooling strip is introduced to the computational domain in between $x = 126.21$ mm and $x = 202.97$ mm for the $0.4 \times T_{ad}$ case with a smooth flat profile. The results show that when the synchronization point appears upstream of the cooling strip, the cooling strip increases the growth rate, which leads to an up to 1.5 time increase in the N-factor diagrams for the corresponding frequencies.

Appendix: Grid Data

The grid used in this study is shared in the GitHub online database[¶] along with the density, velocity, and energy variables of the solution file for the adiabatic case without wall cooling. The grid consists of 64 pieces, which correspond to 64 different output files from each parallel core. Each grid file has a 10-element-long communication layer that is used in the communication between cores. The single file containing all grids is not uploaded because of the size limitation of the GitHub database. The grid is shared in a Tecplot format along with the layout files that show the density contour and the grid. The dimensions of physical coordinates (x, y) are in millimeters, and the solution variables are dimensionless. The nondimensionalization is done by their corresponding freestream values.

Acknowledgments

We acknowledge that the numerical simulations were performed at Oklahoma State University's High Performance Computing Center, which is supported in part through National Science Foundation grant OAC–1531128. We also would like to thank the reviewers for taking the time and effort necessary to review the paper. We sincerely appreciate all of their valuable comments and suggestions, which helped us to improve the quality of the paper.

References

[1] Berry, S., Daryabeigi, K., Wurster, K., and Bittner, R., "Boundary-Layer Transition on X-43A," *Journal of Spacecraft and Rockets*, Vol. 47, No. 6, 2010, pp. 922–934. https://doi.org/10.2514/1.45889

[2] Borg, M., "Laminar Instability and Transition on the X-51A," Ph.D. Dissertation, Aeronautics and Astronautics Engineering, Purdue Univ., West Lafayette, IN, 2009.

[3] Fedorov, A., Malmuth, N., Rasheed, A., and Hornung, H., "Stabilization of Hypersonic Boundary Layers by Porous Coatings," *AIAA Journal.* Vol. 39, No. 4, 2001, pp. 605–610. https://doi.org/10.2514/2.1382

[4] Bowcutt, K., Anderson, J., and Capriotti, D., "Viscous Optimized Hypersonic Waveriders," *25th AIAA Aerospace Sciences Meeting*, AIAA Paper 1987-0272, 1987. https://doi.org/10.2514/6.1987-272

[5] Reed, H., Kimmel, R., Schneider, S., Arnal, D., Reed, H., Kimmel, R., Schneider, S., and Arnal, D., "Drag Prediction and Transition in Hypersonic Flow," *28th Fluid Dynamics Conference*, AIAA Paper 1997-1818, 1997. https://doi.org/10.2514/6.1997-1818

[6] Morkovin, M., "Critical Evaluation of Transition from Laminar to Turbulent Shear Layers with Emphasis on Hypersonically Traveling Bodies," Martin Marietta Corp Research Inst. for Advanced Studies AFFDL-TR-08-149, Baltimore MD, 1969.

[7] Reshotko, E., "Boundary-Layer Stability and Transition," *Annual Review of Fluid Mechanics*, Vol. 8, No. 1, 1976, pp. 311–349. https://doi.org/10.1146/annurev.fl.08.010176.001523

[8] Malik, M., "Numerical Methods for Hypersonic Boundary Layer Stability," *Journal of Computational Physics*, Vol. 86, Feb. 1990, pp. 376–413. https://doi.org/10.1016/0021-9991(90)90106-B

[9] Kovasznay, L., "Turbulence in Supersonic Flow," *Journal of the Aeronautical Sciences*, Vol. 20, No. 10, 1953, pp. 657–674. https://doi.org/10.2514/8.2793

[10] Malmuth, N., Fedorov, A., Shalaev, V., Cole, J., Hites, M., Williams, D., and Khokhlov, A., "Problems in High Speed Flow Prediction Relevant to Control," *2nd AIAA Theoretical Fluid Mechanics Meeting*, AIAA Paper 1998-2695, 1998. https://doi.org/10.2514/6.1998-2695

[11] Fedorov, A., Malmuth, N., Rasheed, A., and Hornung, H., "Stabilization of Hypersonic Boundary Layers by Porous Coatings," *AIAA Journal*, Vol. 39, No. 4, 2001, pp. 605–610. https://doi.org/10.2514/2.1382

[12] Oz, F., Evans, E., Goebel, T., Kara, K., Manimala, J., and Jewell, J., "Interaction of Ultrasonic Acoustic Waves and Metasurface Structures for Hypersonic Boundary-Layer Stability Applications," *Bulletin of the American Physical Society*, Vol. 66, Nov. 2021, Paper 17.

[13] Zhao, R., Liu, T., Wen, C., Zhu, J., and Cheng, L., "Theoretical Modeling and Optimization of Porous Coating for Hypersonic Laminar Flow Control," *AIAA Journal*, Vol. 56, No. 8, 2018, pp. 2942–2946. https://doi.org/10.2514/1.J057272

[14] Brès, G., Inkman, M., Colonius, T., and Fedorov, A., "Second-Mode Attenuation and Cancellation by Porous Coatings in a High-Speed Boundary Layer," *Journal of Fluid Mechanics*, Vol. 726, July 2013, pp. 312–337. https://doi.org/10.1017/jfm.2013.206

[15] Brès, G., Colonius, T., and Fedorov, A., "Acoustic Properties of Porous Coatings for Hypersonic Boundary-Layer Control," *AIAA Journal*, Vol. 48, No. 2, 2010, pp. 267–274. https://doi.org/10.2514/1.40811

[16] Pagliaroli, T., Pagliaro, A., Patané, F., Tati, A., and Peng, L., "Wavelet Analysis Ultra-Thin Metasurface for Hypersonic Flow Control," *Applied Acoustics*, Vol. 157, Jan. 2020, Paper 107032. https://doi.org/10.1016/j.apacoust.2019.107032

[17] Xu, J., Liu, J., Mughal, S., Yu, P., and Bai, J., "Secondary Instability of Mack Mode Disturbances in Hypersonic Boundary Layers over Micro-Porous Surface," *Physics of Fluids*, Vol. 32, No. 4, 2020, Paper 044105. https://doi.org/10.1063/5.0001914

[18] Guo, Q., Li, C., Tu, G., Chen, J., Wan, B., and Liu, Y., "Investigation on the Depth Effects of the Micro-Grooves on the Suppression of the Second Modes in the Hypersonic Boundary Layer," *Journal of Physics: Conference Series*, Vol. 1786, No. 1, 2021, Paper 012053. https://doi.org/10.1088/1742-6596/1786/1/012053

[19] Miller, S., Mamrol, D., Redmond, J., Jantze, K., Scalo, C., and Jewell, J., "High-Speed Boundary Layer Instability on a Flat Plate at Angle of Attack with Porous Walls," *AIAA SciTech 2022 Forum*, AIAA Paper 2022-0303, 2022. https://doi.org/10.2514/6.2022-0303

[20] Rasheed, A., Hornung, H., Fedorov, A., and Malmuth, N., "Experiments on Passive Hypervelocity Boundary-Layer Control Using an Ultrasonically Absorptive Surface," *AIAA Journal*, Vol. 40, No. 3, 2002, pp. 481–489. https://doi.org/10.2514/2.1671

[21] Maslov, A., Shiplyuk, A., Sidorenko, A., Polivanov, P., Fedorov, A., Kozlov, V., and Malmuth, N., "Hypersonic Laminar Flow Control Using

[¶]https://github.com/frkanz/hypersonic_flow_over_cone [retrieved 28 August 2022].

a Porous Coating of Random Microstructure," *44th AIAA Aerospace Sciences Meeting and Exhibit*, AIAA Paper 2006-1112, 2006. https://doi.org/10.2514/6.2006-1112

[22] Fedorov, A., Kozlov, V., Shiplyuk, A., Maslov, A., and Malmuth, N., "Stability of Hypersonic Boundary Layer on Porous Wall with Regular Microstructure," *AIAA Journal*, Vol. 44, No. 8, 2006, pp. 1866–1871. https://doi.org/10.2514/1.21013

[23] Fedorov, A., Shiplyuk, A., Maslov, A., Burov, E., and Malmuth, N., "Stabilization of a Hypersonic Boundary Layer Using an Ultrasonically Absorptive Coating," *Journal of Fluid Mechanics.* Vol. 479, March 2003, pp. 99–124. https://doi.org/10.1017/S0022112002003440

[24] Lees, L., "The Stability of the Laminar Boundary Layer in a Compressible Fluid," NACA TR-876, 1947, pp. 1–49.

[25] Mack, L., "Linear Stability Theory and the Problem of Supersonic Boundary-Layer Transition," *AIAA Journal*, Vol. 13, No. 3, 1975, pp. 278–289.

[26] Mack, L., "Boundary-Layer Linear Stability Theory," Jet Propulsion Lab., California Inst. of Technology AGARD TR 709, Part 3, Pasadena, CA, 1984.

[27] Kara, K., Balakumar, P., and Kandil, O., "Effects of Wall Cooling on Hypersonic Boundary Layer Receptivity over a Cone," *38th Fluid Dynamics Conference and Exhibit*, AIAA Paper 2008-3734, 2008. https://doi.org/10.2514/6.2008-3734

[28] Paquin, L., Skinner, S., and Laurence, S., "Effect of Wall Cooling on the Stability of a Hypersonic Boundary Layer over a Slender Cone," *AIAA Aviation 2021 Forum*, AIAA Paper 2021-2866, 2021. https://doi.org/10.2514/6.2021-2866

[29] Paquin, L., Skinner, S., and Laurence, S., "Boundary-Layer Disturbances and Surface Heat-Flux Profiles on a Cooled Slender Cone," *AIAA SciTech 2022 Forum*, AIAA Paper 2022-1709, 2022. https://doi.org/10.2514/6.2022-1709

[30] Zhu, Y., Gu, D., Zhu, W., Chen, S., Lee, C., and Oran, E., "Dilatational-Wave-Induced Aerodynamic Cooling in Transitional Hypersonic Boundary Layers," *Journal of Fluid Mechanics*, Vol. 911, March 2021, Paper A36. https://doi.org/10.1017/jfm.2020.1044

[31] Oddo, R., Hill, J., Reeder, M., Chin, D., Embrador, J., Komives, J., Tufts, M., Borg, M., and Jewell, J., "Effect of Surface Cooling on Second-Mode Dominated Hypersonic Boundary Layer Transition," *Experiments in Fluids*, Vol. 62, No. 7, 2021, pp. 1–18. https://doi.org/10.1007/s00348-021-03237-0

[32] Masad, J., and Abid, R., "On Transition in Supersonic and Hypersonic Boundary Layers," *International Journal of Engineering Science*, Vol. 33, No. 13, 1995, pp. 1893–1919. https://doi.org/10.1016/0020-7225(95)00046-Z

[33] Polivanov, P., Gromyko, Y., Sidorenko, A., Maslov, A., Keller, M., Groskopf, G., and Kloker, M., "Effects of Local Wall Heating and Cooling on Hypersonic Boundary-Layer Stability," *Proceedings of the Summer Program*, 2011, p. 1.

[34] Soudakov, V., Fedorov, A., and Egorov, I., "Investigations of Laminar-Turbulent Transition on a Sharp Cone with Localized Heating or Cooling in High-Speed Flow," *51st AIAA Aerospace Sciences Meeting Including the New Horizons Forum and Aerospace Exposition*, AIAA Paper 2013-0524, 2013. https://doi.org/10.2514/6.2013-524

[35] Fedorov, A., Soudakov, V., Egorov, I., Sidorenko, A., Gromyko, Y., Bountin, D., Polivanov, P., and Maslov, A., "High-Speed Boundary-Layer Stability on a Cone with Localized Wall Heating or Cooling," *AIAA Journal*, Vol. 53, No. 9, 2015, pp. 2512–2524. https://doi.org/10.2514/1.J053666

[36] Sidorenko, A., Gromyko, Y., Bountin, D., Polivanov, P., and Maslov, A., "Effect of the Local Wall Cooling/Heating on the Hypersonic Boundary Layer Stability and Transition," *Progress in Flight Physics*, Vol. 7, July 2015, pp. 549–568. https://doi.org/10.1051/eucass/201507549

[37] Zhao, R., Wen, C., Tian, X., Long, T., and Yuan, W., "Numerical Simulation of Local Wall Heating and Cooling Effect on the Stability of a Hypersonic Boundary Layer," *International Journal of Heat and Mass Transfer*, Vol. 121, June 2018, pp. 986–998. https://doi.org/10.1016/j.ijheatmasstransfer.2018.01.054

[38] Batista, A., and Kuehl, J., "Local Wall Temperature Effects on the Second-Mode Instability," *Journal of Spacecraft and Rockets*, Vol. 57, No. 3, 2020, pp. 580–595. https://doi.org/10.2514/1.A34620

[39] Chou, A., "Mach-6 Receptivity Measurements of Laser-Generated Perturbations on a Flared Cone," Ph.D. Thesis, School of Aeronautics, Purdue Univ., West Lafayette, IN, 2014.

[40] Liu, X., Osher, S., and Chan, T., "Weighted Essentially Non-Oscillatory Schemes," *Journal of Computational Physics*, Vol. 115, No. 1, 1994, pp. 200–212. https://doi.org/10.1006/jcph.1994.1187

[41] Gottlieb, S., and Shu, C., "Total Variation Diminishing Runge–Kutta Schemes," *Mathematics of Computation*, Vol. 67, No. 221, 1998, pp. 73–85. https://doi.org/10.1090/S0025-5718-98-00913-2

[42] Kara, K., Balakumar, P., and Kandil, O., "Effects of Nose Bluntness on Hypersonic Boundary-Layer Receptivity and Stability over Cones," *AIAA Journal*, Vol. 49, No. 12, 2011, pp. 2593–2606. https://doi.org/10.2514/1.J050032

[43] Anderson, J. D., *Computational Fluid Dynamics: The Basics with Applications*, McGraw–Hill, New York, 1995, pp. 105–125, Chap. 6.

[44] Anderson, D., Tannehill, J. C., and Pletcher, R. H., *Computational Fluid Mechanics and Heat Transfer*, CRC Press, Boca Raton, FL, 2012, pp. 247–343, Chap. 5.

[45] Hoffmann, K. A., and Chiang, S. T., *Computational Fluid Dynamics*, Vol. 1, Engineering Education System, Wichita, KS, 2000, pp. 358–420.

[46] Zhong, X., and Wang, X., "Direct Numerical Simulation on the Receptivity, Instability, and Transition of Hypersonic Boundary Layers," *Annual Review of Fluid Mechanics*, Vol. 44, Jan. 2012, pp. 527–561. https://doi.org/10.1146/annurev-fluid-120710-101208

[47] Rawat, P., and Zhong, X., "On High-Order Shock-Fitting and Front-Tracking Schemes for Numerical Simulation of Shock–Disturbance Interactions," *Journal of Computational Physics*, Vol. 229, No. 19, 2010, pp. 6744–6780. https://doi.org/10.1016/j.jcp.2010.05.021

[48] Kara, K., Balakumar, P., and Kandil, O., "Effects of Nose Bluntness on Stability of Hypersonic Boundary Layers over a Blunt Cone," *37th AIAA Fluid Dynamics Conference and Exhibit*, AIAA Paper 2007-4492, 2007. https://doi.org/10.2514/6.2007-4492

[49] Balakumar, P., "Receptivity of a Supersonic Boundary Layer to Acoustic Disturbances," *AIAA Journal*, Vol. 47, No. 5, 2009, pp. 1069–1078. https://doi.org/10.2514/1.33395

[50] Kara, K., Balakumar, P., and Kandil, O., "Receptivity of Hypersonic Boundary Layers due to Acoustic Disturbances over Blunt Cone," *45th AIAA Aerospace Sciences Meeting and Exhibit*, AIAA Paper 2007-0945, 2007. https://doi.org/10.2514/6.2007-945

[51] Oz, F.,, and , and Kara, K., "Effects of Local Cooling on Hypersonic Boundary-Layer Stability," *AIAA SciTech 2021 Forum*, AIAA Paper 2021-0940, 2021. https://doi.org/10.2514/6.2021-0940

[52] Horvath, T., Berry, S., Hollis, B., Singer, B., and Chang, C., "Boundary Layer Transition on Slender Cones in Conventional and Low Disturbance Mach 6 Wind Tunnels," *32nd AIAA Fluid Dynamics Conference and Exhibit*, AIAA Paper 2002-2743, 2002. https://doi.org/10.2514/6.2002-2743

[53] Kara, K., "Hypersonic Boundary Layer Receptivity to Acoustic Disturbances over Cones," Ph.D. Dissertation, Mechanical and Aerospace Engineering, Old Dominion Univ., Norfolk, VA, 2008, https://doi.org/10.25777/kg7w-c725

[54] Balakumar, P., "Transition in a Supersonic Boundary-Layer Due to Roughness and Acoustic Disturbances," *33rd AIAA Fluid Dynamics Conference and Exhibit*, AIAA Paper 2003-3589, 2003. https://doi.org/10.2514/6.2003-3589

[55] Taylor, G., and Maccoll, J., "The Air Pressure on a Cone Moving at High Speeds," *Proceedings of the Royal Society of London, Series A: Mathematical and Physical Sciences*, Vol. 139, No. 838, Feb. 1933, pp. 298–311. https://doi.org/10.1098/rspa.1933.0018

[56] Jewell, J., and Kimmel, R., "Boundary-Layer Stability Analysis for Stetson's Mach 6 Blunt-Cone Experiments," *Journal of Spacecraft and Rockets*, Vol. 54, No. 1, 2017, pp. 258–265. https://doi.org/10.2514/1.A33619

[57] Paredes, P., Choudhari, M., Li, F., Jewell, J., Kimmel, R., Marineau, E., and Grossir, G., "Nosetip Bluntness Effects on Transition at Hypersonic Speeds," *Journal of Spacecraft and Rockets*, Vol. 56, No. 2, 2019, pp. 369–387. https://doi.org/10.2514/1.A34277

[58] Fedorov, A., and Tumin, A., "High-Speed Boundary-Layer Instability: Old Terminology and a New Framework," *AIAA Journal*, Vol. 49, No. 8, 2011, pp. 1647–1657. https://doi.org/10.2514/1.J050835

[59] Fong, K., Wang, X., and Zhong, X., "Numerical Simulation of Roughness Effect on the Stability of a Hypersonic Boundary Layer," *Computers, and Fluids*, Vol. 96, June 2014, pp. 350–367. https://doi.org/10.1016/j.compfluid.2014.01.009

Downloaded by OKLAHOMA STATE UNIVERSITY on October 28, 2022 | http://arc.aiaa.org | DOI: 10.2514/1.A35404

[60] Fong, K., Wang, X., and Zhong, X., "Parametric Study on Stabilization of Hypersonic Boundary Layer Waves Using 2-D Surface Roughness," *53rd AIAA Aerospace Sciences Meeting*, AIAA Paper 2015-0837, 2015. https://doi.org/10.2514/6.2015-0837

[61] Wang, X., and Zhong, X., "The Stabilization of a Hypersonic Boundary Layer Using Local Sections of Porous Coating," *Physics of Fluids*, Vol. 24, No. 3, 2012, Paper 034105. https://doi.org/10.1063/1.3694808

[62] Wang, X., and Zhong, X., "Role of the Synchronization Point on Boundary Layer Stabilization Using Porous Coating," *38th Fluid Dynamics Conference and Exhibit*, AIAA Paper 2008-4382, 2008. https://doi.org/10.2514/6.2008-4382

[63] Blanchard, A., and Selby, G., "An Experimental Investigation of Wall-Cooling Effects on Hypersonic Boundary-Layer Stability in a Quiet Wind Tunnel," NASA CR-198287, 1996.

[64] Jaffe, N., Okamura, T., and Smith, A., "Determination of Spatial Amplification Factors and Their Application to Predicting Transition," *AIAA Journal*, Vol. 8, No. 2, 1970, pp. 301–308. https://doi.org/10.2514/3.5660

[65] Soudakov, V. G., Egorov, I. V., and Fedorov, A. V., "Computational Studies of Laminar-Turbulent Transition on a Sharp Cone with Local Heating or Cooling," *16th International Conference on the Methods of Aerophysical Research*, Aug. 2012.

[66] Wang, X., Zhong, X., and Ma, Y., "Response of a Hypersonic Boundary Layer to Wall Blowing-Suction," *AIAA Journal*, Vol. 49, No. 7, 2011, pp. 1336–1353. https://doi.org/10.2514/1.J050173

M. Borg
Associate Editor

Downloaded by OKLAHOMA STATE UNIVERSITY on October 28, 2022 | http://arc.aiaa.org | DOI: 10.2514/1.A35404